ELSEVIER

Journal of Fluids and Structures 22 (2006) 505–527

JOURNAL OF FLUIDS AND STRUCTURES

www.elsevier.com/locate/jfs

Amplification and amplitude limitation of heave/pitch limit-cycle oscillations close to the transonic dip

G. Dietz*, G. Schewe, H. Mai

Institut für Aeroelastik des DLR, Bunsenstraße 10, D-37073 Göttingen, Germany

Received 27 May 2005; accepted 22 January 2006
Available online 18 April 2006

Abstract

Recent results from flutter experiments of the supercritical airfoil NLR 7301 at flow conditions close to the transonic dip are presented. The airfoil was mounted with two degrees-of-freedom in an adaptive solid-wall wind tunnel, and boundary-layer transition was tripped. Flutter boundaries exhibiting a transonic dip were determined and limit-cycle oscillations (LCOs) were measured. The local energy exchange between the fluid and the structure during LCOs is examined and leads to the following findings: at supercritical Mach numbers below that of the transonic-dip minimum the presence of a shock-wave and its dynamics destabilizes the aeroelastic system such that the decreasing branch of the transonic dip develops. At higher Mach numbers the shock-wave motion has a stabilizing effect such that the flutter boundary increases to higher flutter-speed indices with increasing Mach number. Amplified oscillations near this branch of the flutter boundary obtain energy from the flow mainly due to the dynamics of a trailing-edge flow separation. A slight nonlinear amplitude dependency of the shock motion and a possibly occurring boundary-layer separation cause the amplitude limitation of the observed LCOs. The impact of the findings on the numerical simulation of these phenomena is discussed.

Keywords: Limit-cycle oscillations; Transonic dip; Flutter; Supercritical airfoil

1. Introduction

The inherently nonlinear transonic flow is assumed to cause two well-known aeroelastic phenomena in the interaction with a typical transport-aircraft structure (Bendiksen, 1992; Schewe et al., 2003): first, in the "transonic dip" (Tijdeman, 1977), the flutter speed shows a noticeable minimum between the critical Mach number where local supersonic regions occur in the flowfield and the Mach number where massive flow separation possibly limits the operational flight regime of an aircraft; secondly, amplitude-limited oscillations of the structure, so-called limit-cycle oscillations (LCOs), may occur (Schewe and Deyhle, 1996) instead of "classical" flutter where exponentially growing and destructive structural oscillations occur at flight speeds above the critical flutter speed. However, the impact of the particular nonlinear aerodynamic mechanisms, such as shock/boundary-layer interaction or flow separation, on the aeroelastic behavior is not as well understood as the impact of structural nonlinearities, e.g. freeplay (Dowell et al., 2003). The understanding

*Corresponding author.
E-mail address: Guido.Dietz@dlr.de (G. Dietz).
URL: http://www.ae.go.dlr.de.

0889-9746/$ - see front matter © 2006 Elsevier Ltd. All rights reserved.
doi:10.1016/j.jfluidstructs.2006.01.004

and the accurate prediction of this nonlinear aeroelastic behavior is expected to play an increasing role in the development of modern aircraft and future air vehicles with probably even higher degrees of structural flexibility than today, e.g. morphing airplanes (Dowell et al., 2003; Schuster et al., 2003). Therefore, in a previous paper, the authors linked the global aerodynamic force behavior to observed transonic-dip phenomena and LCOs (Dietz et al., 2004a). In the present paper, the authors' goal is to provide a more detailed understanding of the local aerodynamic phenomena that cause both the amplification and the amplitude limitation of aeroelastic oscillations close to the transonic dip.

The present study reports results from experiments on heave/pitch LCOs of the supercritical airfoil NLR 7301 with tripped boundary-layer transition at flow conditions close to the transonic dip. Thus, it concentrates on two spatial dimensions since a heaving and pitching airfoil can be seen as a representative section of a wing exhibiting bending and torsional oscillations. The measurements were carried out in the adaptive test section of the Transonic Wind Tunnel Göttingen DNW-TWG. The evaluation of the experimental results contributes to the understanding of both, the amplification and the amplitude limitation of oscillations of an elastic lifting surface in transonic flow. Hints for an appropriate aeroelastic modeling of the experimentally observed phenomena close to the transonic dip are derived and discussed.

2. Recent progresses in understanding transonic aeroelasticity

Here, an analysis of the recent progresses in the literature regarding the physical understanding of the aeroelastic behavior close to the transonic dip is necessary, in order to understand the approach and the results of the present paper.

An overview of the substantial progress in modeling and understanding of nonlinear aeroelastic phenomena was provided by Dowell et al. (2003). A summary of primary aerodynamic and structural dynamic sources which may be responsible for aeroelastic nonlinearities was presented. In addition to freeplay and geometric structural nonlinearities, nonlinear aerodynamic shock-wave motion and/or flow separation are expected to cause nonlinear aeroelastic behavior. The impact of uncertainties in predicting the behavior of a nonlinear aeroelastic system was pointed out: first, in a subcritical bifurcation situation, two response states of the aeroelastic system are possible at the same control parameter and were reported by aircraft operators. Thus, gusts or strong control commands may shift the aeroelastic system from one state without oscillations to another critical state with strong oscillations [so-called "hard flutter"/"explosive LCO" by Thomas et al. (2004)]. Secondly, two nominally identical aircraft were observed to exhibit different aeroelastic responses although there are only tiny differences e.g. in their structural dynamics (Chen et al., 1998; Mignolet et al., 1999). This property is typical nonlinear behavior. According to Schuster et al. (2003) many of today's problems already require aeroelastic analyses that consider nonlinear aero- and structural dynamics. Schuster et al. (2003) stated that future air vehicles will demand aeroelastic and aeroservoelastic methodologies that account for the resulting aeroelastic nonlinearities and take into account the impact of wing thickness and camber and static aeroelastic deformation (Schuster et al., 2003). Computational aeroelasticity (CAE) should encompass and continue to be developed on three levels of complexity: linear methods (e.g. DLM/eigenvalue problems), moderate fidelity methods (e.g. reduced-order modeling) and high-fidelity methods (e.g. RANS/FEM coupling).

The basis for improving or expanding CAE in order to predict nonlinear aeroelastic phenomena is their physical understanding. This understanding is necessary to choose the right modeling and to couple the structural and the aerodynamic models appropriately. Although more accurate and much more efficient theoretical models, e.g. for the nonlinear aerodynamics, are becoming available (Dowell et al., 2003), new insights in the governing physics of nonlinear aeroelastic phenomena are required to make effective and efficient use of the available modeling.

The observations of Bendiksen (2001) regarding the shape of transonic flutter boundaries motivated the numerical studies of Kholodar et al. (2003, 2004a). The behavior of an airfoil mounted with the two degrees-of-freedom (2 dof) in heave and pitch was investigated with an Euler harmonic-balance (HB) method. The reduced velocity of the flutter boundary was presented as a function of Mach number and mass ratio. The sensitivity of the flutter boundary with respect to the structural-dynamic parameters was described and visualized using this three-parameter flutter surface. The similarity parameters of Bendiksen (1999) for airfoils of different thicknesses were successfully tested on the basis of the numerical results. The numerical method was validated by comparison with measured flutter boundaries obtained at the NACA 0012 Benchmark Model of Rivera et al. (1992). For Mach numbers $0.30 \leqslant Ma_\infty \leqslant 0.82$, the numerical and experimental results agreed well. In the range $0.82 < Ma_\infty < 0.88$, no experimental data were published by Rivera et al. (1992) and the HB method revealed no flutter boundary for the considered values of mass ratio and speed of sound (Kholodar et al., 2004a). At higher Mach numbers, $0.88 \leqslant Ma_\infty \leqslant 0.95$, the numerical and experimental results disagree. The disagreement was suspected to be caused by viscous effects which

could not be taken into account by the Euler HB method, although the experiments indicate strong shock-induced separation at these conditions.

The authors presumed that arranging the steady flowfield appropriately may cause unsteady flow that does not lead to a pronounced transonic dip (Dietz et al., 2004a). This idea was investigated by Dietz et al. (2004b): a computational lift-constrained airfoil-shape optimization was conducted with the two objectives to minimize the drag as well as the upstream propagation time of pressure disturbances in the steady flowfield above the airfoil for a given transonic Mach number and a given Reynolds number. It was shown that this multi-objective minimization reduced the phase lag of the lift response to a harmonic pitch motion of the optimized airfoil compared with the initial airfoil. Moreover, the optimized airfoil had a better steady aerodynamic performance. Flutter calculations based on a transonic doublet-lattice method (TDLM) by Voß (1985) and Lu and Voß (1993) showed that the flutter boundary of the optimized airfoil exhibited higher flutter-speed indices compared with the initial airfoil. The optimized airfoil had only 53% thickness of the initial airfoil. Thus, this flutter-behavior dependency on the airfoil thickness in principal matched the observation of Kholodar et al. (2004a) while comparing the flutter boundaries of a NACA 0004 with that of a NACA 0012. However, it was demonstrated that TDLM was not able to capture the increasing branch of the flutter boundary at Mach numbers higher than that of the transonic-dip minimum. The TDLM method was applied on the basis of steady solutions of the coupled Euler/boundary-layer equations using MSES by Drela and Giles (1987) and Drela (1990). Although these steady state solutions included a prediction of the separated boundary-layer on the airfoil, the flutter-speed indices of the flutter boundary decreased monotonously in the TDLM prediction even at Mach numbers higher than that of the expected transonic-dip minimum. This paper will discuss this observation based on the experimental results in Section 4.4.

Kholodar et al. (2004b) studied, in addition to the flutter boundary, also the LCO behavior of the NACA 0012 Benchmark Model of Rivera et al. (1992) with the Euler HB method. The effect of the uncoupled heave to pitch frequency ratio was investigated at a Mach number where the experiments did not report massive flow separation. For a given LCO amplitude, the reduced velocities exhibited a minimum near a frequency ratio of one. Below that ratio, an attractor and supercritical bifurcation behavior was detected, whereas well above a ratio of one a repeller and subcritical bifurcation behavior was found. It was demonstrated that the LCO behavior is very sensitive to the Mach number and that the aeroelastic nonlinearity was prominent only in a limited range of transonic Mach numbers. However, the results did not take into account viscosity, which is likely to play an important role at high Mach numbers due to shock/boundary-layer interaction and flow separation. Thomas et al. (2004) demonstrated this strong impact of viscosity on the LCO behavior numerically by results of an HB approach applying a solver of the Euler equations compared with a solver of the Reynolds-averaged Navier–Stokes equations. The simulations for the NLR 7301 airfoil were compared with the test case MP77 [Knipfer and Schewe (1999); corrected structural-dynamic parameters in Schewe et al. (2003)] occurring at a Mach number close to the transonic-dip minimum. The viscous effects led to a supercritical LCO behavior with respect to reduced velocity while the inviscid model predicts more or less exponentially growing amplitudes. However, like other computational methods (Weber et al., 2001; Castro et al., 2001; Tang et al., 2003), this approach also predicted much higher LCO amplitudes than the ones which were experimentally observed. Castro et al. (2001) took into account the presence of the porous wind-tunnel walls of MP77. It was shown that modeling the wind-tunnel wall porosity significantly affects the LCO characteristics. These results confirmed the authors' former decision to avoid this additional challenge in simulation by providing well-defined boundary conditions in terms of an adaptive test section (Wedemeyer et al., 1998) for the recent experiments (torsion flutter in Schewe et al., 2002; Dietz et al., 2004a). Thomas et al. (2003) simulated the torsion flutter in transonic flow observed by Schewe et al. (2002) in the adaptive test section. A maximum in the magnitude of the computed first harmonic of the pitching moment for a Mach number of 0.7711 was interpreted as wind-tunnel resonance with a frequency of 70 Hz. It was believed that this "wind-tunnel resonance condition is responsible for the flutter onset total pressure dip" (Thomas et al., 2003, p. 6). However, the observed phenomenon does not match the lowest wind-tunnel resonance frequency of 106 Hz, which is here estimated by the method of Voß (1998), for the same flow conditions. Furthermore, the torsion flutter was experimentally observed only with boundary-layer transition tripping; without tripping, no flutter case could be found at this flow conditions (Schewe et al., 2002). Additionally, a frequency of 70 Hz matches typical buffet frequencies observed at NLR 7301 models in the Transonic Wind Tunnel Göttingen DNW-TWG (Schewe et al., 2002). Thus, Thomas et al. (2003) most likely have identified an aerodynamic instability of the flow around the airfoil instead of a wind-tunnel resonance.

Similar to Birnbaum (1924), Patil (2003) discusses wing flutter and flapping flight based on the energy transfer mechanisms between flow and structure that result in drag or propulsion. Three types of modes were identified for an aeroelastic system: an unstable flutter mode with an increase in drag, a stable mode with an increase in drag, and a stable flapping-flight mode generating thrust. It was stated that the energy needed to amplify flutter oscillations comes from the propulsive unit and is transferred via the flow to the structure. Since flutter oscillations induce drag while the

thrust in trimmed flight may be kept constant, the aircraft should be decelerated. The oscillation amplitude of the wing, and thus its drag, alters with the airspeed reduction such that limit-cycle oscillations may occur even while assuming linear aero- and structural-dynamics (Patil, 2002).

The authors also investigated the energy exchange between the fluid and the structure, namely while an airfoil exhibits LCOs in transonic flow (Dietz et al., 2004a). This approach led to insights into the amplification and amplitude limitation mechanisms based on the behavior of the global aerodynamic loads lift and pitching-moment. In particular, the experiments on heave/pitch flutter of a supercritical airfoil NLR 7301 in transonic flow led to the following findings: a very slight nonlinear dependency of the unsteady aerodynamic loads on the amplitude of the airfoil motion was responsible for the amplitude limitation of the flutter oscillations close to the transonic dip. Due to this slight nonlinearity, LCOs could be controlled by relatively small forces, but LCO amplitudes also strongly depended on the damping of the aeroelastic systems. The time lag of the lift response to the airfoil pitch motion has driven the oscillations and appeared to cause the characteristic shape of the transonic dip. The observations matched those of Bendiksen (1992) stating that in transonic flow the phase difference between heave and pitch motion tends to adjust such that single degree-of-freedom (sdof) flutter occurs. Bendiksen (1992) argued that the work during one oscillation cycle contributed by the lift due to the shock motion is maximized in this case. Bendiksen (2004) performed an analysis of limit-cycle flutter phenomena, focusing on the identification of amplitude-limiting mechanisms from a global energy-exchange perspective. Based on theoretical considerations he emphasized that CAE needs to model the energy exchange between the fluid and the structure correctly and with a sufficient spatial and temporal accuracy in order to predict LCO amplitudes. Contrarily to above mentioned publications, Bendiksen (2004) simulated in Euler-based calculations, small-amplitude LCOs which matched the experimental data of MP77 surprisingly well. It was stated that, in the absence of flow separation, a transition from sinusoidal shock-wave motion (Tijdeman and Seebass, 1980, Type A) to interrupted shock-wave motion (Type B) appears to cause the amplitude limitation. With this kind of transition from Type A to Type B shock motion occurring on the suction and the pressure side of an nonsymmetrical airfoil section at different oscillation amplitudes, Bendiksen (2004) expected two nested LCOs to occur. Nevertheless, he believed that intermittent trailing-edge boundary-layer separation caused by shock/boundary-layer interaction has a similar effect as that of a transition from Type A to Type B shock-wave motion.

Motivated by this recent progress, realized by the inspection of the energy transfer (Dietz et al., 2004a; Bendiksen, 2004), and the advances gained by interpreting the local work coefficient in turbomachinery (Grüber and Carstens, 2001), the present paper provides new insights to transonic flutter based on the local energy exchange between the fluid and the structure.

3. Set-up

Detailed information about the flutter-test set-up and the test procedures can be found in Schewe et al. (2002) and Dietz et al. (2004a). Only details regarding an improved set-up used in the present investigation and details which are important in order to understand the reported results are presented here.

3.1. Wind tunnel

The present wind-tunnel investigation was carried out in the Transonic Wind Tunnel Göttingen DNW-TWG operated by the foundation German–Dutch Wind Tunnels. The DNW-TWG is a continuously working facility with a $1\,\mathrm{m} \times 1\,\mathrm{m}$ adaptive test-section. The stagnation temperature in this wind tunnel is kept constant by a closed-loop control of a cooler, while Mach number and stagnation pressure may be varied independently. A given inflow Mach number is also kept constant by a closed-loop control using the measured ratio of the static pressure to the stagnation pressure in the test-section. The diffuser cross-section downstream of the test-section is adapted such that the inflow velocity is held constant. Therefore, the observed LCOs cannot be caused by such mechanisms as described by Patil (2002). The ratio of the wind-tunnel height to the chord of the investigated airfoil model is 3.333. Therefore, the top and bottom walls were adapted to the stationary flow at the mean angle of attack of the airfoil, where the static aeroelastic equation is satisfied. The wall interference is minimized by a one-step method of wall adaptation based on a Cauchy type integral (Wedemeyer et al., 1998). The displacement thickness of the turbulent wind-tunnel wall boundary layer is predicted by Head's method (Cebeci and Bradshaw, 1979) and is added to the wall shapes; top and bottom wall displacement thicknesses are obtained according to the measured pressure gradients at each wall while the gradient is neglected for the sidewalls (Jacobs, 2002). This adaptation to the mean steady position of the airfoil yields nearly a minimum residual wall interference for a moderately oscillating airfoil, as shown in pretests (Jacobs, 2002). The lowest

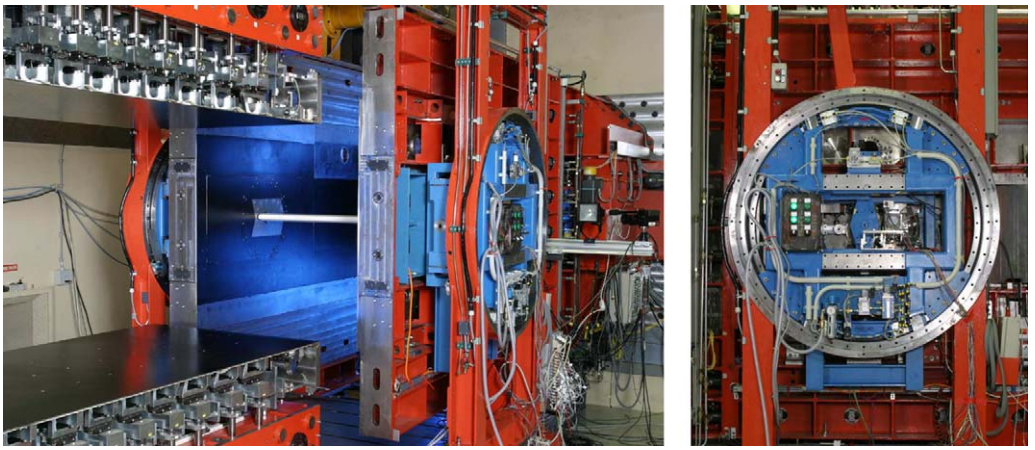

Fig. 1. Pictures of the improved flutter-test set-up with installed airfoil model mounted in the adaptive test section of the DNW-TWG. The adaptive test-section is opened.

value for the wind-tunnel resonance frequency can be estimated using the method of Voß (1998): based on this method, the ratio of flutter to wind-tunnel resonance frequency is lower than 30%, and the ratio of buffeting to wind-tunnel resonance frequency is lower than 77% for the reported data.

3.2. Flutter-test set-up

The applied set-up allows free heave and pitch motions of the airfoil model for flutter tests. A theoretical model representing the structural dynamics of this set-up is described in Section 3.4. The mean angle of attack $\bar{\alpha}$ of the aeroelastic system under airloads depends on the structural-dynamic parameters, the off-wind angle of attack α_0 and the flow parameters. The off-wind angle of attack α_0 can only be adjusted with high efforts while the wind tunnel is shut down.

Contrary to the formerly used flutter-test set-up [cf. Tichy and Henke (1993), Schewe et al. (2002), Dietz et al. (2004a)], the entire improved flutter-test set-up can be rotated with α_{2D} around the elastic axis of the aeroelastic system in order to tune the angle of attack to a given value while the wind tunnel is running (see Fig. 1, right). Thus, a target mean angle of attack $\bar{\alpha}$ can be fine-tuned while the static aeroelastic equilibrium is fulfilled. During the present tests, the angle of the complete set-up with respect to the flow direction was $-0.74^\circ \leqslant \alpha_{2D} \leqslant 0.32^\circ$. Of course, the heave direction of the aeroelastic system with respect to the flow direction changes also with the amount of α_{2D}. But, the error in the heave-motion data perpendicular to the flow direction is lower than 0.01% and the amount of edgewise motion due to the nonzero α_{2D} is less than 1.3% compared with the heave amplitude.

In the flutter-test set-up, the airfoil is mounted on each side to a piezoelectric balance of high stiffness (Schewe, 1991) in order to measure the steady and unsteady lift, drag and pitching moment. Two laser triangulators on each side of the wind tunnel measure the instantaneous heave and pitch of the model. A control system may introduce forces in heave direction which are also measured piezoelectrically. A digital signal-processor device derives the heave velocity from the laser-triangulator signals such that a voltage proportional to this velocity can be passed into one electrodynamical exciter on each side. Small heave motions of the airfoil can then either be amplified or damped, by applying the inverted signal. Tests revealed that in open-loop state this flutter control system can be seen as nonintrusive. The set-up, with the airfoil model mounted in the adaptive test section of the DNW-TWG, is shown in Fig. 1.

3.3. Airfoil model

The airfoil model was shaped as the supercritical NLR 7301 airfoil with the contour given by Zwaan (1979), except that this geometry was cut off at $x/c = 1$. Thus, the trailing edge of the model is blunt, with approximately 0.1% chord. In the present investigation the chord meets the leading and trailing edge of the model so that the given angle-of-attack α differs from the NLR results by $\alpha = \alpha_{\mathrm{NLR}} - 0.183^\circ$. The model is made of a carbon-fiber composite structure having a chord of $c^* = 0.3\,\mathrm{m}$ and a span of $b^* = 1\,\mathrm{m}$. It is lightweight and very stiff so that the natural frequencies of the

flutter-test set-up and the flutter frequencies are well below the first deformation natural frequency of the airfoil model. Accordingly, it is appropriate to treat the airfoil model as rigid.

In order to investigate the unsteady flow around the oscillating airfoil, the model is equipped with 64 miniature differential pressure transducers (Kulite XCQ-093-5psiD) measuring both steady and unsteady pressure differences with respect to the pressure in the DNW-TWG plenum. These sensors are arranged beneath the model surface and the pressure taps are located in a zig-zag pattern of ±0.5% span around the middle section at 50% span. In each of three laterally distributed sections of the airfoil model, two accelerometers (PCB 352C22) are mounted in the model, one near the leading edge, the other close to the trailing edge. The measured data were recorded by the AMIS II data acquisition system, which is capable of sampling the signals of 360 channels simultaneously at up to 44 kHz per channel and with 16 bit resolution.

Laminar-turbulent boundary-layer transition was tripped at 7% chord on the suction and 14% chord on the pressure side by zig-zag tape with a height of 0.0467% chord. The effectiveness of the transition tripping was checked by infrared imaging in former experiments with the same set-up and similar flow conditions. The tripping was applied in the attempt of obtaining a better comparison with numerical simulations, since the accurate prediction of the transition region is still an unsolved problem, in particular for unsteady flows.

3.4. Structural-dynamic model of the flutter-test set-up

The heave and pitch motions of the airfoil in the flutter-test set-up are modeled by a 2 dof system as shown in Fig. 2. The corresponding equations of motion can be written in nondimensional form as

$$v_\infty^2 \mathbf{M}\frac{\partial^2 \mathbf{u}(t)}{\partial t^2} + 2v_\infty \mathbf{D}\frac{\partial \mathbf{u}(t)}{\partial t} + \mathbf{K}\mathbf{u}(t) = \frac{2}{\pi}\frac{v_\infty^2}{\mu}\mathbf{f}(t), \tag{1}$$

where

$$\mathbf{M} = \begin{bmatrix} 1 & -x_\alpha \\ -x_\alpha & r_\alpha^2 \end{bmatrix}, \quad \mathbf{D} = \begin{bmatrix} \delta_h \omega_h/\omega_\alpha & 0 \\ 0 & \delta_\alpha r_\alpha^2 \end{bmatrix}, \quad \mathbf{K} = \begin{bmatrix} (\omega_h/\omega_\alpha)^2 & 0 \\ 0 & r_\alpha^2 \end{bmatrix},$$

$$\mathbf{f}(t) = \begin{bmatrix} c_l(t) \\ c_m(t) + x_0 c_l(t) \end{bmatrix} \quad \text{and} \quad \mathbf{u}(t) = \begin{bmatrix} h(t) \\ \alpha(t) - \alpha_0 \end{bmatrix}.$$

Eq. (1) describes the motion of the airfoil, its nondimensional heave $h(t) = h^*(t)/c^*$ at the elastic axis, as well as the difference between its angle of attack $\alpha(t)$ and its off-wind value α_0, which depend on the nondimensional time

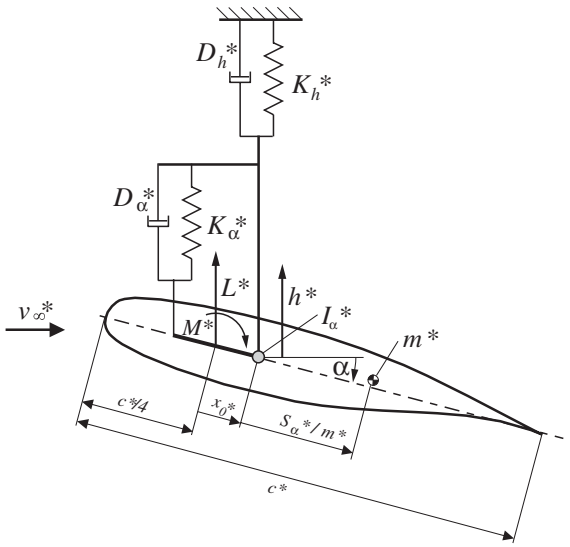

Fig. 2. Schematic of the structural model.

$t = t^* v_\infty^*/c^*$. With the dimensional quantities of chord length c^*, mass m^*, static mass moment S_α^*, mass moment of inertia I_α^*, spring constants $K_{\alpha/h}^*$, and damping coefficients $D_{\alpha/h}^*$, as well as the free-stream speed v_∞^* and density ρ_∞^*, the structural-dynamic parameters are made nondimensional as follows:

$$\begin{aligned}
&\text{elastic axis to } \tfrac{1}{4}\text{-chord point distance: } x_0 = x_0^*/c^* = 0.0,\\
&\text{elastic axis to center of mass distance: } x_\alpha = S_\alpha^*/m^* c^* = 0.0429,\\
&\text{radius of gyration about the elastic axis: } r_\alpha = \sqrt{I_\alpha^*/m^* c^{*2}} = 0.2102,\\
&\text{Lehr' s pitch-damping coefficient: } \delta_\alpha = D_\alpha^*/2\sqrt{K_\alpha^* I_\alpha^*} = 0.13\%,\\
&\text{Lehr' s heave-damping coefficient: } \delta_h = D_h^*/2\sqrt{K_h^* m^*} = 0.38\%,\\
&\text{uncoupled natural frequency ratio: } \omega_h/\omega_\alpha = \sqrt{K_h^*/m^*}/\sqrt{K_\alpha^*/I_\alpha^*} = 0.6886.
\end{aligned} \tag{2}$$

The aerodynamic lift $L^*(t)$ and pitching moment $M^*(t)$ that act on the airfoil with span b^* through the $\frac{1}{4}$-chord point can be nondimensionalized as

$$\begin{aligned}
&\text{lift coefficient: } c_l(t) = L^*(t) \Big/ \left(\tfrac{1}{2}\rho_\infty^* v_\infty^{*2} c^* b^*\right),\\
&\text{moment coefficient: } c_m(t) = M^*(t) \Big/ \left(\tfrac{1}{2}\rho_\infty^* v_\infty^{*2} c^{*2} b^*\right).
\end{aligned} \tag{3}$$

The reciprocal of the reduced pitching natural frequency $k_\alpha = \sqrt{K_\alpha^*/I_\alpha^*}c^*/v_\infty^* = 70.35\,\mathrm{m/s}/v_\infty^*$ can be interpreted as a nondimensional free-stream speed $v_\infty = 1/k_\alpha$ and is called the reduced speed. The reduced frequency $k = \omega^* c^*/v_\infty^*$ is made nondimensional with the full chord length c^*. The mass ratio $\mu = (m^*/(\pi/4 c^{*2} b^*))/\rho_\infty^* = 429.22\,\mathrm{kg/m^3}/\rho_\infty^*$ describes the ratio of the structural inertial forces to the aerodynamic loads, whereas the flutter-speed index $\mathrm{fi} = 2\mathrm{v}_\infty/\sqrt{\mu}$ characterizes the ratio of the aerodynamic loads to the elastic forces.

The above structural-dynamic parameters of the improved flutter-test set-up were obtained at $\alpha_0 = 0^\circ$ and $\alpha_{2D} = 0^\circ$. The chord length, mass and torsional-spring constant, were measured directly. The mass moment of inertia, the static mass moment and the bending-spring constant were measured and then corrected by the results of a ground vibration test (GVT). The correction procedure minimizes the discrepancies between the theoretically obtained eigenfrequencies and maximizes the collinearity of the eigenvectors to the values that were measured. The relative difference between the eigenfrequencies of the structural model without aerodynamic loads to those of the GVT is smaller than 0.2%, the collinearity of the eigenvectors is greater than 99.4%. The relative error of the measured eigenfrequencies is very small whereas the damping constants may be obtained from the GVT with a relative error of $\mathcal{O}(20\%)$.

4. Results and discussion

The presented data were measured in the flutter-test set-up while the airfoil model was allowed to oscillate freely in the flow. Flutter boundaries were determined at three different angles of attack. Two LCO cases close to the transonic dip were selected in order to discuss the amplification and the amplitude limitation of the oscillations. One LCO case was measured at a supercritical Mach number, lower than that of the transonic-dip minimum; the other at a Mach number close to the buffeting boundary. These two new LCO cases differ from the authors' previous LCO test cases (Dietz et al., 2004a): they were obtained at other structural-dynamic parameters and the model here was equipped with pressure transducers. The time-dependent pressure data combined with the motion data of the model allowed an examination of the local energy exchange between the fluid and the structure.

4.1. Transonic dip and limit-cycle oscillation cases

Fig. 3 shows the measured flutter and buffeting boundaries for three different angles of attack in the flutter-speed index fi/Mach-number (Ma_∞) plane. The corresponding data are reported in Table 1. At stable conditions below the flutter boundary, the aeroelastic system was excited by the flutter-control system such that damping coefficients could be determined from the decaying oscillation amplitudes in the recorded time traces. Analogously, at unstable conditions above the flutter boundary the negative damping coefficients, i.e. the amplification rates of the observed oscillations, were determined from the time traces. The square symbols show data from test series at a fixed stagnation pressure where the Mach number was varied from stable conditions until amplified oscillations of the airfoil occurred. The zero

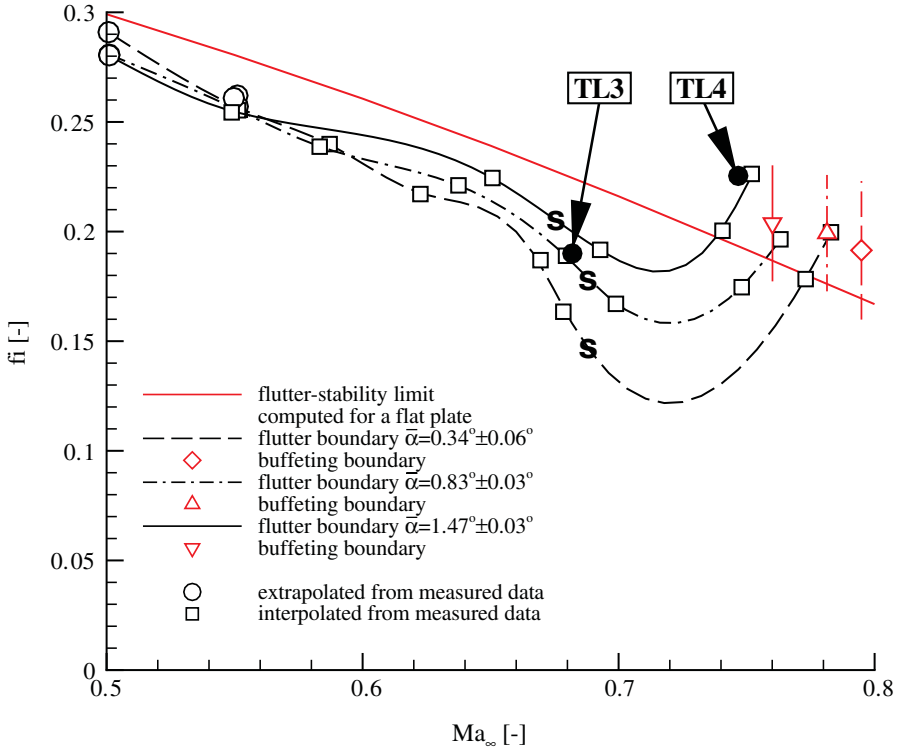

Fig. 3. Comparison of measured flutter and buffeting boundaries at $Su_0 = 110.4\,K/T_0^* = 0.362 \pm 1.7\%$ with a flutter-stability limit analyzed from theoretically obtained derivatives for a flat plate. Simulations predict trailing-edge separation with respect to increasing Mach number at conditions marked by an "s" (cf. discussion of Fig. 8).

Table 1
Measured flutter and buffeting boundaries at $Su_0 = 110.4\,K/T_0^* = 0.362 \pm 1.7\%$

$\bar{\alpha} = 0.34^\circ \pm 0.06^\circ$				$\bar{\alpha} = 0.83^\circ \pm 0.03^\circ$				$\bar{\alpha} = 1.47^\circ \pm 0.03^\circ$			
Ma_∞	$\frac{Re_\infty}{10^6}$	fi	μ	Ma_∞	$\frac{Re_\infty}{10^6}$	fi	μ	Ma_∞	$\frac{Re_\infty}{10^6}$	fi	μ
Extrapolated flutter boundary											
0.501	4.00	0.291	302.0	0.501	4.05	0.281	295.7	0.501	3.88	0.280	316.1
0.551	3.20	0.262	419.9	0.551	3.08	0.257	436.3	0.550	3.21	0.261	414.8
Interpolated flutter boundary											
0.552	3.06	0.256	440.2	0.551	3.04	0.255	442.3	0.549	3.05	0.254	439.5
0.587	2.58	0.240	557.5	0.583	2.55	0.239	559.3	0.651	2.11	0.224	761.7
0.623	2.01	0.217	761.0	0.637	2.05	0.221	762.6	0.693	1.45	0.192	1178.7
0.669	1.43	0.187	1154.2	0.679	1.43	0.189	1170.9	0.741	1.50	0.200	1223.8
0.678	1.08	0.163	1559.7	0.699	1.07	0.167	1599.3	0.752	1.88	0.226	987.8
0.773	1.16	0.178	1661.6	0.748	1.14	0.175	1624.6				
0.783	1.45	0.200	1346.0	0.763	1.14	0.196	1625.1				
Buffeting boundary											
0.795	1.31	0.191	1524.5	0.781	1.43	0.199	1358.2	0.760	1.53	0.204	1230.4

passing of the damping coefficients being interpolated over Mach number illustrates the flow conditions of the flutter boundary. The circle symbols show data which are extrapolated from tests at stable conditions of an identical Mach number but at different stagnation pressures. Here the damping coefficients were extrapolated over the flutter-speed

index such that the flutter-speed index with zero damping could be estimated. The data obtained by both methods at $Ma_\infty \approx 0.55$ in Fig. 3 agree well. The flutter-boundary data obtained for approximately the same incidence are connected by Akima (1970) splines. Unfortunately, the lower limit of the stagnation pressure $p_0^* > 30\,\mathrm{kPa}$ achievable at DNW-TWG and the limited available time for the entire test campaign did not allow a precise identification of the transonic-dip minimum. Accordingly, these spline curves must not be over-interpreted in terms of the precise transonic-dip minimum locations. Nevertheless, the variation of the angle of attack for a single measured flutter boundary could be reduced from $\pm 0.13^\circ$ (Dietz et al., 2004a) down to $\pm 0.03^\circ$ by use of the improved flutter-test set-up. Furthermore, the test time to obtain one flutter boundary was reduced significantly. However, the variation in Mach number and stagnation pressure corresponds to a variation of the Reynolds number since the stagnation temperature and thus the Sutherland constant $Su_0 = 110.4\,\mathrm{K}/T_0^*$ in the DNW-TWG wind tunnel was held constant by a closed-loop controlled cooler. This variation of the Reynolds number is documented in Table 1.

At high Mach numbers, the combined heave/pitch oscillations with a typical reduced frequency of $k \approx 0.2$ changed to pitch dominated oscillations at $k \approx 0.5$ which match neither structural eigenfrequencies nor wind-tunnel resonance frequencies. In former tests with the NLR 7301, buffet with $k = 0.56$ was identified at $Ma_\infty = 0.75$ and a fixed incidence of $\alpha = 2.40^\circ$. Thus, in the present tests buffeting was assumed to occur at these flow conditions which are also shown in Fig. 3 and listed in Table 1. With increasing angle of attack the Mach number of the buffeting boundary decreases. This behavior is typical for the buffet onset (Stanewsky, 1990), since the Mach number at which flow separation, and its unsteady interaction with strong shock waves above the suction side of an airfoil, is expected to occur decreases with increasing incidence.

Fig. 3 also shows a flutter-stability limit of an infinitesimal thin flat plate in inviscid but compressible flow [cf. Dietz et al. (2004a) using the method of Carstens (1973)], which is elastically mounted with the structural dynamics according to Eqs. (1) and (2). At low Mach numbers, the measured data at the NLR 7301 and the theoretical results for the flat plate agreed well. At Mach numbers $Ma_\infty > 0.66$, the flutter boundaries start to disagree significantly. At Mach numbers lower than that of the transonic-dip minimum, the measured flutter-speed indices of the flutter boundary were lower than that of the flat plate. At Mach numbers close to the buffeting boundary, the measured aeroelastic system gets even more stable than that of the flat plate indicated by higher measured flutter-speed indices.

Several conditions in the unstable region of the transonic dip above the flutter boundary were found where LCOs occurred. Qualitatively and quantitatively, the manifestations of these LCOs agree to the observations by Schewe et al. (2003) and Dietz et al. (2004a). Two LCO cases called TL3 and TL4 were selected for further investigations. Both cases were found to be representative for the aeroelastic behavior on each branch of the transonic dip in the present tests. The flow and the structural parameters of these LCO cases are reported in Table 2. Furthermore, the location of these cases in the flutter-speed index/Mach number plane is shown in Fig. 3. Both cases were measured very close to, but above the flutter boundary in the unstable region of the flutter-speed-index/Mach-number plane. TL3 occurred at a supercritical Mach number below that of the transonic-dip minimum, while TL4 was close to the buffeting boundary. TL3 represents a situation where the flutter-speed index is lower than that of the flat plate. The aeroelastic system at TL4 was more stable than the elastically mounted flat plate. In both cases a phase difference of $\phi_\alpha - \phi_h \approx 180^\circ$ was observed between the pitch and the heave motion. Therefore, these LCOs can also be interpreted as a sdof motion as observed and discussed by the authors for the formerly obtained test cases TL1 and TL2 (Dietz et al., 2004a).

Figs. 4 and 5 show on the left side the time traces of the pitch $\alpha(t)$ and the heave $h(t)$ motion as they were measured for TL3 and TL4 by the laser triangulators. First, the aeroelastic system was artificially stabilized by the flutter control

Table 2
Limit-cycle oscillation cases TL3 and TL4

Flow and structural parameters			Measured LCO properties		
	TL3	TL4		TL3	TL4
Ma_∞	0.677	0.751	$\bar{\alpha}$	1.05°	1.46°
$Re_\infty/10^6$	1.43	1.88	$\bar{c}_l$	0.348	0.454
Su_0	0.364	0.360	$\bar{c}_m$	−0.059	−0.067
μ	1164.5	989.0	$\hat{h}$	0.27%	0.19%
v_∞	3.21	3.56	$\hat{\alpha}$	0.17°	0.10°
α_0	$1.51^\circ \pm 0.03^\circ$	$2.18^\circ \pm 0.04^\circ$	$\hat{h}/\hat{\alpha}$	0.89	1.08
			$\phi_\alpha - \phi_h$	176°	175°
			k	0.220	0.203

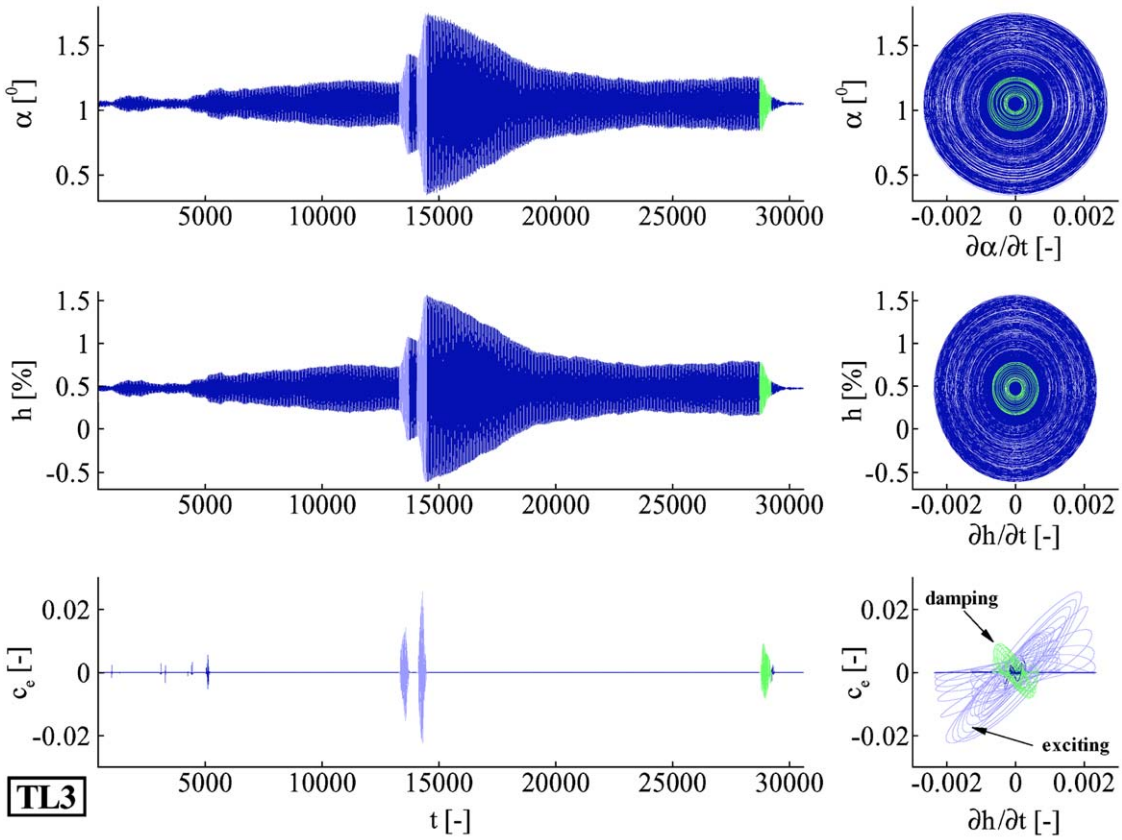

Fig. 4. Limit-cycle oscillation case TL3. Left: time traces of the pitch α and the heave h motion as well as the exciter-force coefficient $c_e(t) = F_e^*(t)/(\frac{1}{2}\rho_\infty^* v^{*2} c^* b^*)$. Right: corresponding phase-space representation. $\mathrm{Ma}_\infty = 0.677$, $\mathrm{Re}_\infty = 1.43 \times 10^6$, $\mathrm{Su}_0 = 0.364$, $\mu = 1164.5$, $v_\infty = 3.21$, $\alpha_0 = 1.51^\circ \pm 0.03^\circ$.

system. In both cases, this system was switched off in open-loop state shortly before the depicted time traces started. Slowly, the pitch and heave amplitudes grew to their stable LCO value. Obviously, the LCO observed in TL4 does not exhibit such a constant amplitude compared with TL3. In both cases, during the recorded time traces, the flutter-control system was used to increase the oscillation amplitudes in order to ensure that the observed LCOs were stable. The forces which were applied by the electrodynamic exciters in the heave direction are shown in the lower part of Figs. 4 and 5. They are presented as exciter-force coefficients, nondimensionalized in the same manner as the lift coefficient. At the end of the depicted time traces, the same flutter-control system was used to damp out the oscillations. Like in former tests (Dietz et al., 2004a), the exciter-force coefficients needed to control the state of the aeroelastic system were remarkably small compared with a typical lift coefficient of 0.4. On the lower right of Figs. 4 and 5, the exciter-force coefficient is plotted against the instantaneous heave velocity. This demonstrates that, during the excitation of the oscillations, the flutter-control system induces forces which are in phase with the heave velocity. For the damping, a 180° phase shift is applied.

4.2. Steady flow properties close to the limit-cycle oscillation cases

As shown in the foregoing, the oscillations of the aeroelastic system in TL3 and TL4 could be damped out by use of the flutter-control system. For those sections of the time traces where the system was nearly at rest, steady-state pressure distributions were determined by time averaging the measured pressure data. These measured pressure distributions of TL3 and TL4 are presented in Fig. 6. They are shown together with pressure and skin-friction distributions that are obtained by integrating the coupled Euler- and boundary-layer equations by using the code MSES of Drela and Giles (1987), assuming free-flight farfield boundary conditions. For both simulated cases, Mach Ma_∞ and Reynolds number

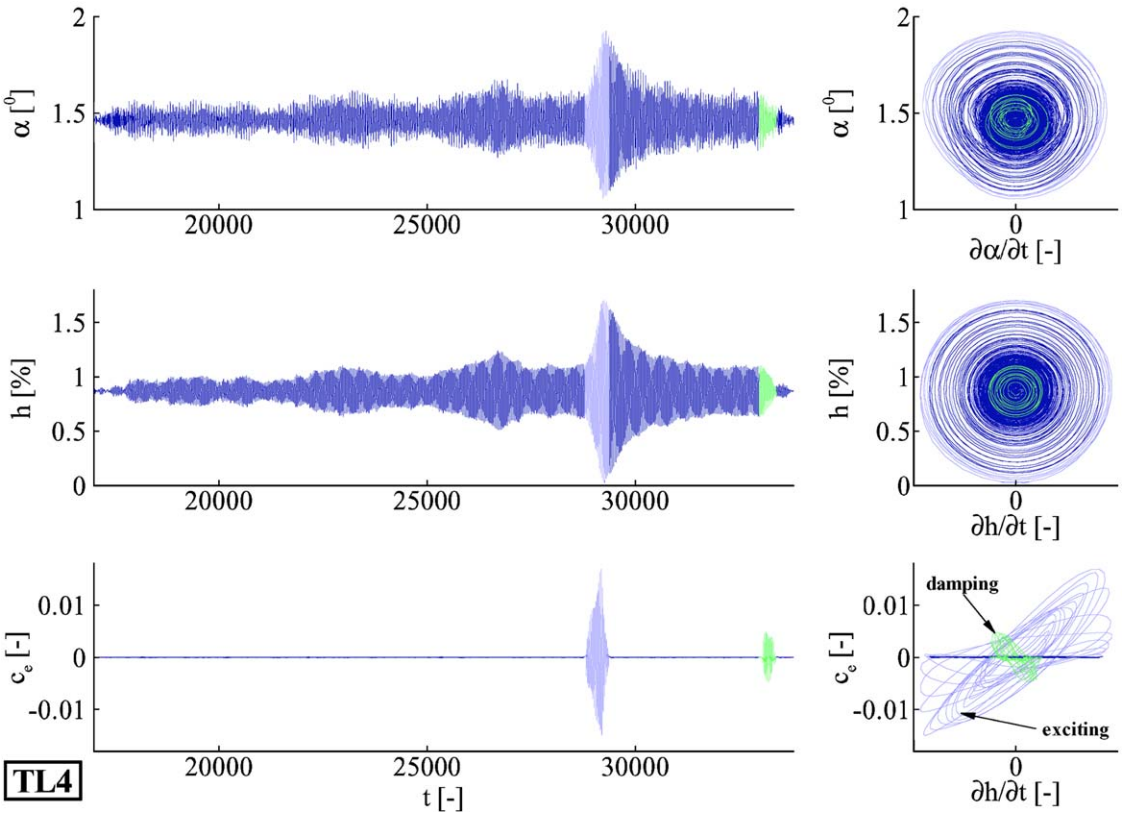

Fig. 5. Limit-cycle oscillation case TL4. Left: time traces of the pitch α and the heave h motion as well as the exciter-force coefficient $c_e(t)$. Right: corresponding phase-space representation. $\mathrm{Ma}_\infty = 0.751$, $\mathrm{Re}_\infty = 1.88 \times 10^6$, $\mathrm{Su}_0 = 0.360$, $\mu = 989.0$, $v_\infty = 3.56$, $\alpha_0 = 2.18^\circ \pm 0.04^\circ$.

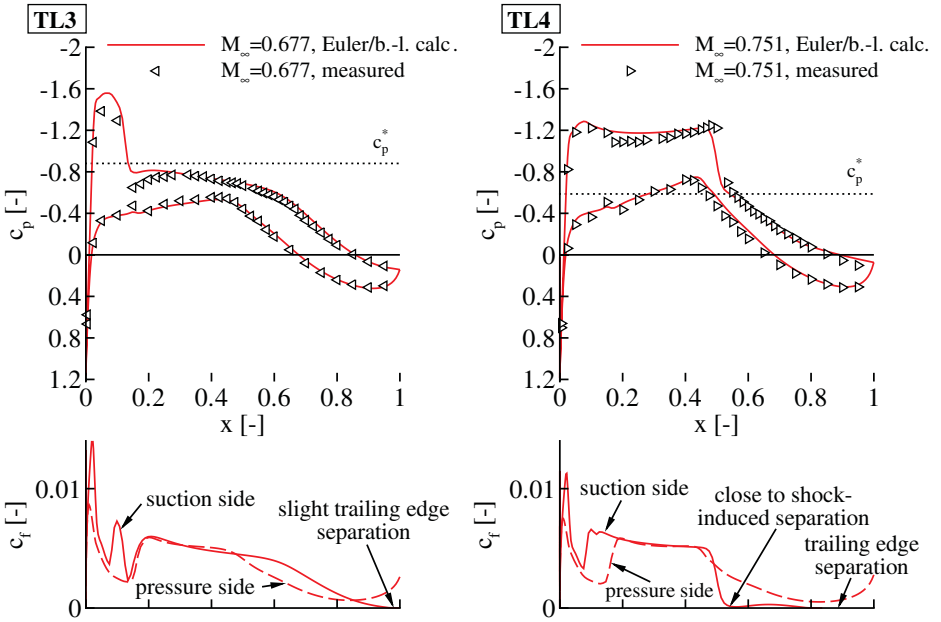

Fig. 6. Measured steady-state pressure distributions $c_p(x)$ of TL3 and TL4 compared with pressure and skin-friction $c_f(x)$ distributions simulated with the Drela and Giles (1987) Euler/boundary-layer code MSES. Left: $\mathrm{Ma}_\infty = 0.677$, $\mathrm{Re}_\infty = 1.43 \times 10^6$, $\mathrm{Su}_0 = 0.364$, $\alpha = 1.05^\circ$. Right: $\mathrm{Ma}_\infty = 0.751$, $\mathrm{Re}_\infty = 1.88 \times 10^6$, $\mathrm{Su}_0 = 0.360$, $\alpha = 1.46^\circ$.

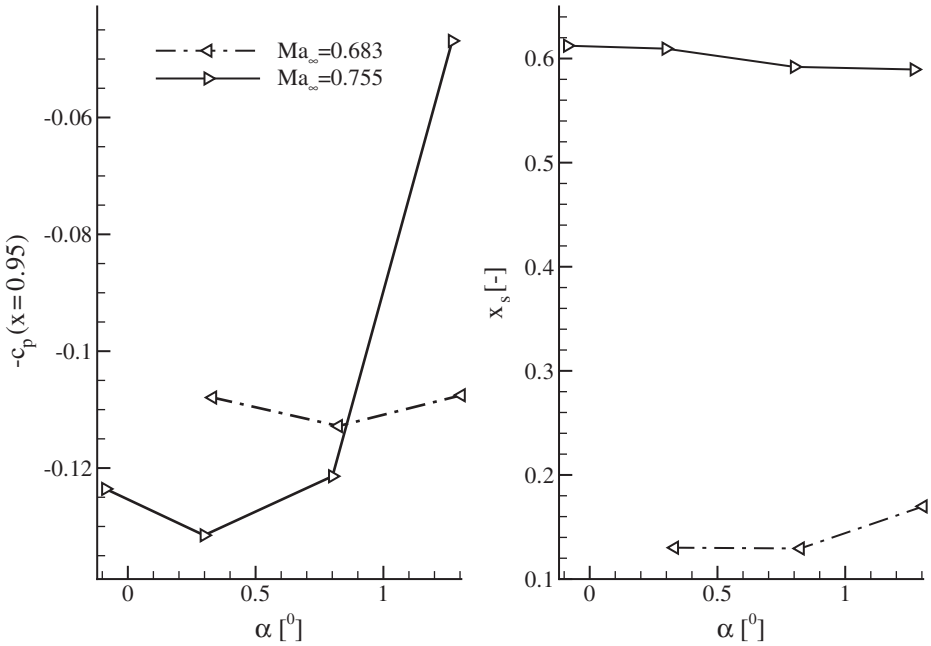

Fig. 7. Measured dependency of the pressure coefficient near the trailing edge $c_p(x = 0.95)$ (left) and the shock-location x_s (right) on the angle of attack α at flow conditions close to the cases TL3 and TL4. Dash-dotted lines: $\mathrm{Ma}_\infty = 0.683 \pm 0.2\%$, $\mathrm{Re}_\infty = 2.15 \times 10^6 \pm 0.3\%$, $\mathrm{Su}_0 = 0.362 \pm 0.2\%$. Solid lines: $\mathrm{Ma}_\infty = 0.755 \pm 0.1\%$, $\mathrm{Re}_\infty = 2.26 \times 10^6 \pm 0.2\%$, $\mathrm{Su}_0 = 0.360 \pm 0.1\%$.

Re_∞ as well as angle of attack α are taken as measured without any corrections. The measured and the simulated pressure distribution match fairly well. Also the pressure recovery at the trailing edge is predicted satisfyingly in both cases. This agreement of the pressure distributions indicates again the effectiveness of the wind-tunnel wall adaptation (Dietz et al., 2004a). For TL3 the entire flow seems to be attached except for a very slight separation near the trailing edge on the suction side, as indicated by the left skin-friction distribution in Fig. 6. The skin-friction distribution in the right of Fig. 6 corresponding to TL4 shows that a trailing-edge separation occurs at $x = 83\%$ and that the suction-side boundary-layer flow is close to a shock-induced separation. So, as also observed by Schewe et al. (2003), a type B separation seems to be present according to the classification of Pearcy et al. (1968), which is expected to be rather sensitive to the Reynolds number and the transition location (Tijdeman, 1977). This should be considered in possible numerical simulations.

The unsteady aerodynamics is assumed to determine strongly the aeroelastic behavior of the system under consideration. In order to understand the unsteady aerodynamics for TL3 and TL4, it is helpful to have a closer look at the quasi-steady separation and shock-location dependency on the angle of attack for a constant Mach number. Fig. 7 shows on the left side a strong rise in the negative pressure coefficient $-c_p(x = 0.95)$ measured near the trailing edge at flow conditions close to that of the case TL4. This indicates a strong thickening of the boundary layer at the trailing edge (Stanewsky, 1990). This indication, together with the skin-friction distribution of Fig. 6, confirms that trailing-edge separation occurs for TL4 in the experiment. Due to this separation, the airfoil is effectively decambered and thus the shock moves upstream with increasing angle of attack (Stanewsky, 1990). Fig. 7 compares on the right side the measured shock locations with respect to the angle of attack. The shock locations were estimated by interpolating the measured pressure distributions over the airfoil-surface arc length using Akima (1970) splines and detecting the location where the interpolation crosses the critical $c_p^*(\mathrm{Ma}_\infty)$ value. The shock locations in Fig. 7 demonstrate that for the case TL3 the shock wave moves aft with increasing incidence, and vice versa for the case TL4.

The dependency of the shock-wave location and the trailing-edge boundary-layer separation on the Mach number is shown in Fig. 8. The data are obtained by using the Drela and Giles (1987) Euler/boundary-layer code MSES. The flow conditions were interpolated from those of the measured flutter-stability limits which are listed in Table 1. A random examination confirmed that the measured and simulated steady-state pressure distributions match fairly well as demonstrated in Fig. 6. The shock locations were estimated by searching the location where the interpolated pressure distributions cross the critical $c_p^*(\mathrm{Ma}_\infty)$ value. The boundary-layer separation points were detected from the

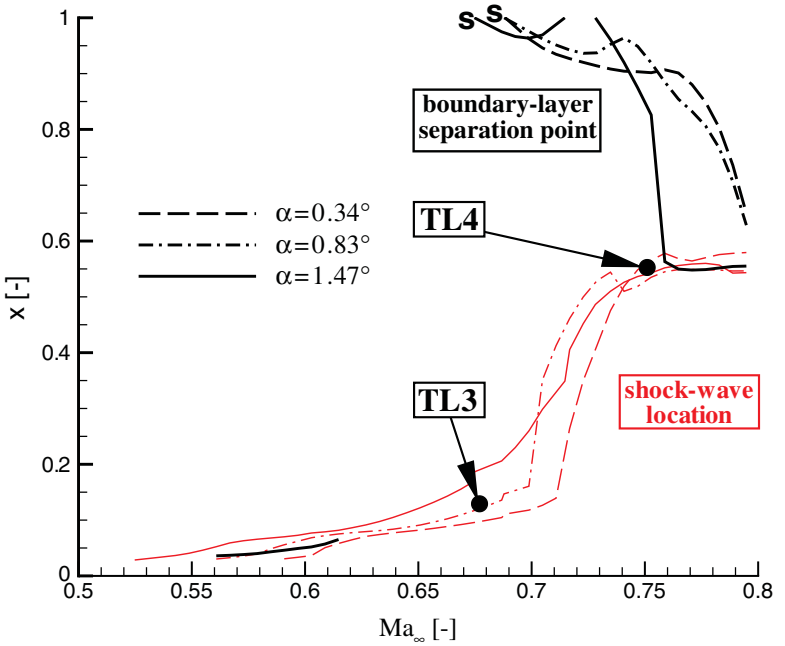

Fig. 8. Dependency of the shock-wave location and the trailing-edge boundary-layer separation on the Mach number according to simulations with the Drela and Giles (1987) Euler/boundary-layer code MSES. The curves correspond to the flow conditions of the measured flutter-stability limits which are listed in Table 1.

skin-friction distributions by searching for $c_f(x) = 0$. Fig. 8 demonstrates, as expected, that the occurrence of a trailing-edge separation impacts the shock location. For all three angles of attack, the Mach number which corresponds to the beginning of a trailing-edge separation is marked by an "s" in Fig. 8 as well as Fig. 3. The beginning of a trailing-edge separation with respect to Mach number seems to correspond to an inflection point in the flutter-stability limit. This might be an indicator of the relevance of flow separation to the shape of the transonic dip and will be discussed in more detail in Section 4.3.

Keeping these steady flow properties in mind, the amplification and the amplitude limitation of the LCO cases TL3 and TL4 is discussed in the following by analyzing the local energy exchange between the fluid and the structure.

4.3. Local energy exchange in limit-cycle oscillations

The energy exchange between the fluid and the structure was previously examined by the authors in order to link the global aerodynamic force behavior to the observed LCOs (Dietz et al., 2004a). The sum of the kinetic energy in the heave and the pitch motion E_{kin} together with the potential energy in the springs E_{pot} must be equal to the constant initial energy $E_0 = E_0^*/(\frac{1}{2}\rho_\infty^* v_\infty^{*2} c^{*2} b^*)$ in the structural-dynamic system plus the sum of work ΣW. Energy is dissipated due to the structural damping with the power $P_v = P_v^*/(\frac{1}{2}\rho_\infty^* v_\infty^{*3} c^* b^*)$. The global aerodynamic loads lift and the pitching moment perform the energy exchange between flow and structure at $P_l + P_m$ per unit time. In addition to this, the flutter-control system puts the power ($P_e > 0$) in or takes the power ($P_e < 0$) out of the structural-dynamic system. Accordingly,

$$E_0 = E_{\text{kin}} + E_{\text{pot}} - W = E_{\text{kin}} + E_{\text{pot}} - \int (P_v + P_l + P_m + P_e)\,\mathrm{d}t \tag{4}$$

is an integral of the equation of motion (1) and thus describes the energy balance for the 2 dof system around its steady position $\tilde{u}$. It was shown that the structural-dynamic parameters of the test set-up, the time traces of the motion, and the forces could be measured with sufficient accuracy in order to evaluate the energy exchange between the fluid and the structure (Dietz et al., 2004a).

In the present paper the local energy exchange between the fluid and the structure is examined on basis of the time-dependent pressure distribution c_p measured in the mid-section of the airfoil model. The skin-friction contribution to

the energy exchange during LCOs is assumed to be small compared with the energy exchange based on the pressure distribution and thus neglected. The heave $h(t)$ and the pitch $\alpha(t)$ motion of the model in the mid-section is evaluated by combining the two corresponding accelerometer signals integrated twice over time. Since the model is assumed to be rigid, the kinematic velocity due to the heave and the pitch motion of the model surface with its coordinates $\mathbf{x}_m = (x_m, z_m)^{\mathrm{T}}$ in the model-fixed coordinate system is

$$\mathbf{v}(\mathbf{x}_m, t) = \frac{\partial h(t)}{\partial t}\begin{bmatrix} -\sin\alpha(t) \\ \cos\alpha(t) \end{bmatrix} + \frac{\partial \alpha(t)}{\partial t}\begin{bmatrix} z_m \\ (x_0 + 0.25) - x_m \end{bmatrix}. \tag{5}$$

The local work coefficient c_W describes the local work per area which is performed by the flow on a surface element $\mathrm{d}A_m$ of the airfoil with the surface-normal vector $\mathbf{n}_m$ during one oscillation period T, i.e.

$$c_W(\mathbf{x}_m, t) = \frac{1}{\mathrm{d}A_m}\int_{t-T/2}^{t+T/2} \underbrace{-(c_p(\mathbf{x}_m, t) - \bar{c}_p(\mathbf{x}_m))\mathbf{n}_m\,\mathrm{d}A_m}_{\text{unsteady pressure force vector}} \mathbf{v}(\mathbf{x}_m, t)\,\mathrm{d}t. \tag{6}$$

Thus, a positive local work coefficient $c_W > 0$ means that the moving structure locally receives energy from the flow and vice versa. If the flow in the wind tunnel would be ideally 2-D, its integral about the airfoil surface along the arc-line elements $\mathrm{d}s$ should be equal to the work performed by the global aerodynamic loads lift and pitching moment

$$\frac{1}{c}\oint c_W(\mathbf{x}_m, t)\,\mathrm{d}s \stackrel{!}{=} \int_{t-T/2}^{t+T/2} (P_l(t) + P_m(t))\,\mathrm{d}t. \tag{7}$$

A comparison of the left-hand (lhs) and the right-hand side (rhs) terms of Eq. (7), applying the wind-tunnel data, shows that the magnitude of the energy exchange between the fluid and the structure in the midsection (lhs term) is nearly the same but generally slightly higher compared with the global energy exchange (rhs term). One reason for the difference may be the neglect of the skin-friction contribution. However, most likely the flow in the present wind-tunnel experiments is close to but not ideally 2-D. Since the global energy evaluation, based on the balance measurement, averages over the entire span, the flow near the wind-tunnel sidewalls is also taken into account. Thus, the magnitude of the work performed during one oscillation cycle near the sidewalls is probably lower than that in the midsection due to the wall interference. However, the evaluation of the energy exchange using the local work coefficient from the measured data seems to exhibit a sufficient accuracy and provides some enlightenment regarding the local aerodynamics causing the amplification and the amplitude limitation of LCOs close to the transonic dip. Therefore, time traces of the local work coefficient for TL3 and TL4 are compared.

Fig. 9 shows the local work coefficient c_W against the airfoil-surface arc lengths and allows one to distinguish between the suction and the pressure side. An arc length of zero represents the leading edge, while a positive arc length represents the suction side and a negative one the pressure side, respectively. The local work coefficient in Fig. 9 is normalized by the instantaneous heave amplitude squared $\hat{h}^2$. The heave rather than the pitch is chosen here since, with the heave motion, the lift feeds the main part of the energy from the flow into the structure. However, normalizing with the pitch amplitude squared $\hat{\alpha}^2$ would yield the same qualitative results. The normalization is done for two reasons: first, to compare the TL3 and TL4 cases, which exhibit different heave amplitudes (cf. Table 2); second, to compare and time-average two different sections of each time trace. In one section, the aeroelastic system exhibits growing amplitudes toward the stable LCO (beginning of the time traces in Figs. 4 and 5). In the second section, the amplitudes shrink down to the stable LCO immediately after the oscillations were artificially increased by the flutter-control system (middle of the time traces in Figs. 4 and 5). The normalization of the local work coefficient by the instantaneous heave amplitude squared $\hat{h}^2$ demonstrates the nonlinear discrepancy between both sections of the time traces more clearly.

The left side of Fig. 9 demonstrates that the shock motion feeds the main part of the energy in the oscillations of TL3. Moreover, the amplitude dependency of the shock motion is responsible for the amplitude limitation of the observed LCOs. That is to say, the peak of the local work coefficient near the time-averaged shock location is smaller when the amplitudes shrink to the LCO amplitude. Although it is somewhat wider, the integral of the local work coefficient about the airfoil surface (cf. Eq. (7)) is slightly lower compared with the section of the time trace where the amplitudes grow to the LCO amplitude. This slightly lower aerodynamic work contribution is enough that the structural damping can cause the oscillation amplitude to decay back to the stable LCO amplitude where the aerodynamic work contribution and the structural damping losses are in balance.

The situation is quite different for TL4 which is shown on the right side of Fig. 9. The shock motion in TL4 is responsible for taking energy out of the aeroelastic system. The higher the oscillation amplitudes the higher the relative energy extraction due to the shock motion. The amplification is contributed to mainly by the trailing-edge flow separation on the airfoil suction side. Although the energy contribution due to the trailing-edge separation increases

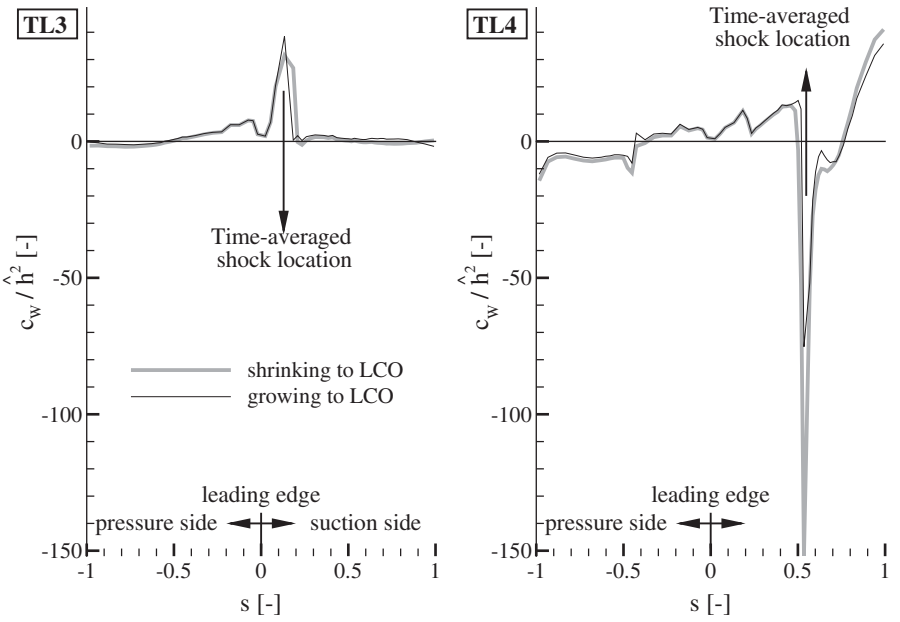

Fig. 9. Local work coefficient c_W normalized by the heave amplitude squared $\hat{h}^2$ against airfoil-surface arc length. Left: TL3, $\mathrm{Ma}_\infty = 0.677$, $\mathrm{Re}_\infty = 1.43 \times 10^6$, $\mathrm{Su}_0 = 0.364$, $\mu = 1164.5$, $v_\infty = 3.21$, $\alpha_0 = 1.51° \pm 0.03°$. Right: TL4, $\mathrm{Ma}_\infty = 0.751$, $\mathrm{Re}_\infty = 1.88 \times 10^6$, $\mathrm{Su}_0 = 0.360$, $\mu = 989.0$, $v_\infty = 3.56$, $\alpha_0 = 2.18° \pm 0.04°$.

when the amplitudes shrink down to the LCO value, this contribution cannot compensate the over-proportional losses due to the shock motion. Thus, the aerodynamic work contribution is lower than in the case of growing amplitudes. This small difference determines whether or not the losses due to structural damping are over-compensated and oscillations are amplified.

Hence, slight nonlinear amplitude dependencies of the shock-motion characteristics and possibly occurring flow separation cause the amplitude limitation of the observed LCOs. Since these amplitude dependencies will cause also a slight nonlinear oscillation-amplitude dependency of the lift and the pitching moment, this observation agrees well with the previous findings of the authors' (Dietz et al., 2004a). It is also obvious that the "stability" of the presented stable LCOs is rather weak. There are only small differences between the energy exchange while the amplitudes grow toward the LCO or while the aeroelastic system falls back to the LCO. This makes clear why LCOs can be controlled by relatively small forces [cf. end of Section 4.1 and Dietz et al. (2004a)].

The impact of the shock-wave motion for TL3, which is located at a Mach number below that of the transonic-dip minimum, is different from TL4 which is close to the buffeting boundary. The shock-wave motion causes a pressure distribution on the oscillating airfoil which leads to an incremental lift. For TL3 this incremental lift exhibits such a phase shift from the heave motion of the airfoil that aerodynamic work is contributed due to the shock motion and oscillations are amplified. This observation matches the results of Bendiksen (1992). Moreover, this destabilizing effect of shock waves decreases with increasing oscillation amplitude, which causes the amplitude limitation at TL3. However, close to the buffeting boundary at a Mach number higher than that of the transonic-dip minimum, the shock wave exhibits a stabilizing effect in TL4. The amplification for TL4 is mainly related to the trailing-edge flow separation on the suction side.

The shock-wave motion around its time averaged position for both LCO cases TL3 and TL4 is presented in Fig. 10. Again, for each case the two different sections of the time traces, i.e. growing and shrinking to the stable LCO, are shown separately. Both plot coordinates are normalized by the heave amplitude $\hat{h}$ in order to demonstrate the nonlinear dependency of the shock motion on the oscillation amplitude. The shock locations were estimated by interpolating the measured pressure distributions of every sample in the time trace over the airfoil-surface arc length using Akima (1970) splines and detecting the location where this interpolation crosses the critical $c_p^*(\mathrm{Ma}_\infty)$ value. The plots of Fig. 10 should not be over-interpreted, since the spatial resolution of the pressure taps particularly near the shock location of TL3 is limited (cf. Fig. 6, left).

Nevertheless, there is a clear difference between the shock motion for TL3 and for TL4: the transfer function estimates a phase difference at the flutter frequency between the shock x_s and the heave h motion which amounts

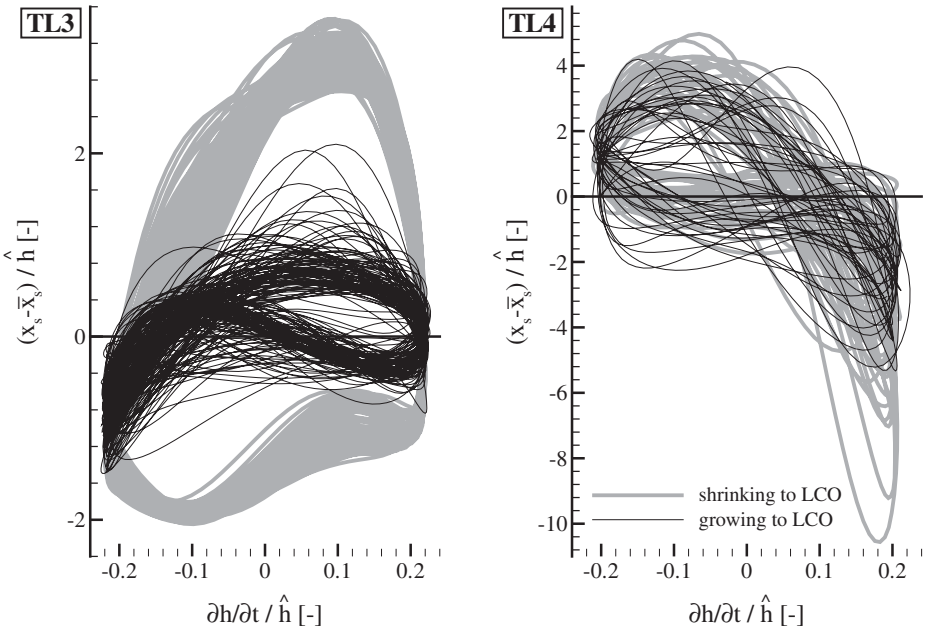

Fig. 10. Shock-wave location x_s against heave velocity, both coordinates are normalized by the heave amplitude $\hat{h}$. Left: TL3, $Ma_\infty = 0.677$, $Re_\infty = 1.43 \times 10^6$, $Su_0 = 0.364$, $\mu = 1164.5$, $v_\infty = 3.21$, $\alpha_0 = 1.51^\circ \pm 0.03^\circ$. Right: TL4, $Ma_\infty = 0.751$, $Re_\infty = 1.88 \times 10^6$, $Su_0 = 0.360$, $\mu = 989.0$, $v_\infty = 3.56$, $\alpha_0 = 2.18^\circ \pm 0.04^\circ$.

$\phi_{x_{sl}} - \phi_h \approx -225^\circ$ for TL3. Contrarily, the phase difference is $\phi_{x_{sl}} - \phi_h \approx -120^\circ$ for TL4. This shift of 105° in the phase differences causes the sign change of the mean slope of the trajectories shown in Fig. 10. It explains that the shock motion causes a work contribution in the one case and energy extraction in the other case. This principal behavior could be expected for moderate motion frequencies from the steady shock-wave behavior shown on the right side of Fig. 7, since for TL4 an inverse shock motion was identified.

Regarding the amplitude limitation mechanism, only the right side of Fig. 10 provides obvious information. The amount of energy exchanged between fluid and structure is expected to be maximal when the shock wave, and thus the resulting lift contribution, is extreme at the maximum or minimum heave velocity. For TL4 on the right side of Fig. 10, the downstream shock location tends to be minimal, close to the maximum heave velocity in the upstroke, heave motion of the airfoil. The shock position is here even more upstream when the amplitudes shrink from a higher level down to the stable LCO. Thus, during the upstroke, power is given locally from the structure to the flow since the lift of the airfoil is close to its minimum while the airfoil heave velocity is at its maximum. For the downstroke motion, no obvious difference between the two sections of the TL4 time trace can be identified. The left side of Fig. 10 only demonstrates that there is a clear amplitude dependency of the shock-motion characteristics. However, the downstream shock location and thus the lift contribution of the shock wave is maximal during the upstroke, and is minimal during the downstroke such that the shock motion causes the transfer of power from the fluid to the structure (cf. Fig. 9).

Fig. 9 demonstrated for TL4 that the amplification is mainly caused by the trailing-edge boundary-layer separation on the suction side of the airfoil. The Euler/boundary-layer simulation presented in Fig. 6 predicts this trailing-edge separation to occur downstream of $x = 83\%$. Therefore, the transfer function of the pressure tap data at $x = 80\%$ to the pressure coefficients c_p downstream of the separation location is estimated. The amplitude ratio $|c_p/c_{p\ x=0.8}|$ (left) and the time delay $(\phi_{c_{p\ x=0.8}} - \phi_{c_p})/k$ (right) of this transfer function estimate, for the fundamental motion frequency k, is plotted against x in Fig. 11. These data are plotted for TL3 and TL4 as well as two cases of forced pitch oscillations at different frequencies, which were measured at a higher Mach number but at a lower angle of attack compared with TL4, such that a boundary-layer separation occurs near the same location of TL4. Both cases of forced pitch oscillations were measured in a previous test campaign. The dash-dotted line of the negative time delay for case TL3, which is expected to exhibit no strong trailing-edge separation, indicates that pressure waves travel and transport information from the trailing-edge upstream. In all other cases, the time delay shown in the right side of Fig. 11 is positive. In both cases of forced pitch oscillations, the time delay is nearly identical although the reduced frequency differs from $k \approx 0.10$

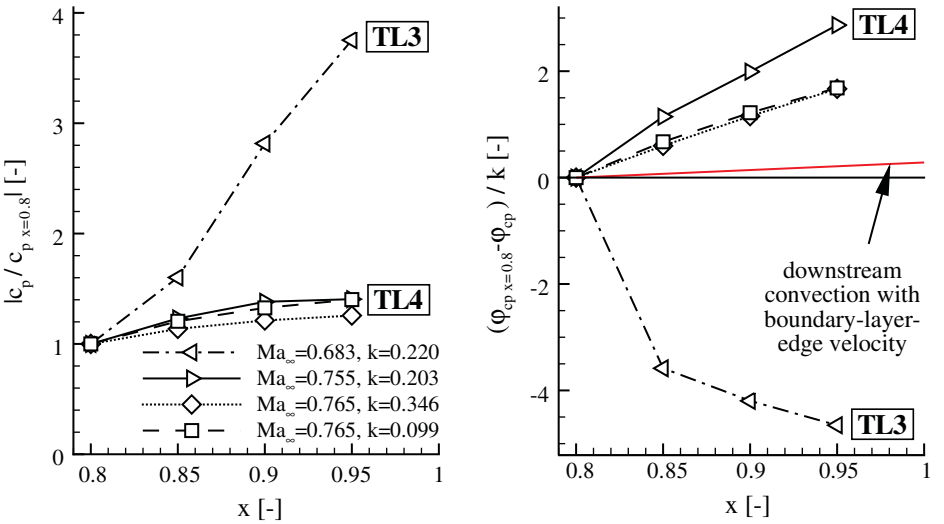

Fig. 11. Amplitude ratio $|c_p/c_{p\ x=0.8}|$ (left) and time delay $(\phi_{c_{p\ x=0.8}} - \phi_{c_p})/k$ (right) of the pressure coefficient c_p response at the fundamental motion frequency k compared with the pressure tap at $x = 0.8$ versus x. Dash-dotted lines: TL3. Solid lines: TL4. Dotted lines: forced pitch oscillations, $\mathrm{Ma}_\infty = 0.765$, $\mathrm{Re}_\infty = 2.28 \times 10^6$, $\mathrm{Su}_0 = 0.359$, $\alpha = 0.80^\circ \pm 0.04^\circ$, $\hat{\alpha} = 0.24^\circ$, $k = 0.346$. Dashed lines: forced pitch oscillations, $\mathrm{Ma}_\infty = 0.765$, $\mathrm{Re}_\infty = 2.28 \times 10^6$, $\mathrm{Su}_0 = 0.359$, $\alpha = 0.80^\circ \pm 0.04^\circ$, $\hat{\alpha} = 0.21^\circ$, $k = 0.099$.

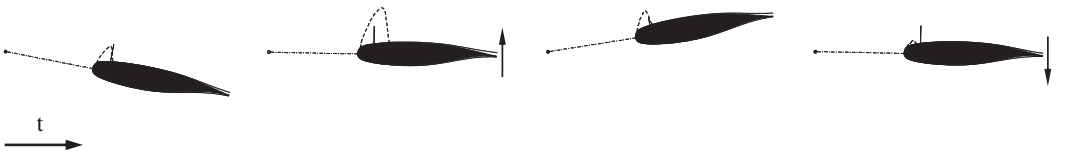

Situation at Mach numbers lower than that of the transonic-dip minimum.

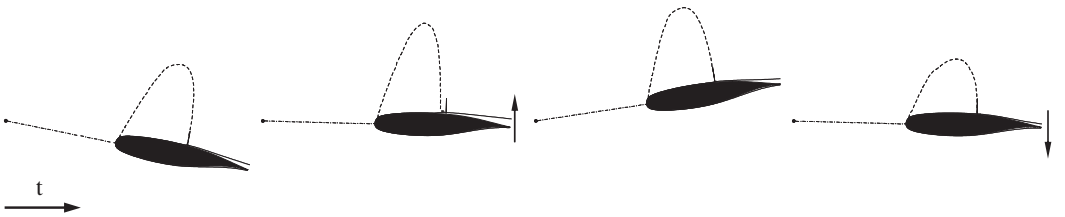

Situation at Mach numbers higher than that of the transonic-dip minimum.

Fig. 12. Single degree-of-freedom (sdof) flutter close to the transonic dip. The time increases from left to right. Thin dashed lines mark the sonic boundaries in the flowfield, thin solid lines indicate the boundary-layer thickness, arrows mark the motion direction.

to $k \approx 0.35$. An attached boundary layer is governed by the outer inviscid flowfield. Downstream of the so-called Goldstein singularity at the point of separation, the region of reverse flow grows and the separation strongly determines the outer flowfield. A boundary-layer separation starts at zero in terms of wall distance. If the separation point moves along the airfoil surface in unsteady flow, the region of reverse flow will most likely develop downstream with a speed between zero and the boundary-layer-edge speed. In all three cases with flow separation, the average flow speed above the boundary-layer edge is about $v = 71\% v_\infty$. The time delay assuming pure downstream convection with this boundary-layer-edge speed is also shown in Fig. 11. This time delay amounts about 10% of that which is found for the time delay $(\phi_{c_{p\ x=0.8}} - \phi_{c_p})/k$ in separated flow.

It should be noted that in the left side of Fig. 11 the amplitude ratios for the cases with separated flow amount approximately one. The behavior observed here might motivate a simple boundary-layer separation model which could be implemented in unsteady aerodynamic simulation methods like TDLM by Voß (1985) or Lu and Voß (1993).

The observations of the present investigation are concluded in the principle drawings of Fig. 12. The upper part of Fig. 12 shows the situation at a supercritical Mach number which is lower than that of the transonic-dip minimum. The observed Sdof flutter mode of the 2dof aeroelastic system exhibits a virtual center of rotation upstream of the airfoil at $\hat{h}/\hat{\alpha}$ [cf. Dietz et al. (2004a)]. The drawings show from the left to the right: the bottom dead center, the up-stroke, the top dead center, and the downstroke during one oscillation cycle. The thin solid lines above the airfoil indicate the boundary-layer thickness. The thin dashed lines mark the sonic boundary. A time-averaged shock-wave location is indicated by a short thin dotted line which is drawn perpendicular to the airfoil chord line. In the upper part of Fig. 12, the shock wave reaches its maximum downstream position during the upstroke. Thus, the lift reaches its temporal maximum and the airfoil is accelerated toward its top dead center. During the downstroke, the situation is opposite. A situation at a supercritical Mach number, which is higher than that of the transonic-dip minimum and close to the buffeting boundary, is depicted in the lower part of Fig. 12. During the upstroke the shock wave reaches its maximum upstream position caused by flow separation. Therefore the shock-wave motion acts to stabilize against the oscillation. But, the boundary layer on the suction side of the airfoil dynamically separates, which leads to an increase of the downstream contribution of the lift such that it drives the oscillation (cf. positive local work coefficient near the trailing edge of the airfoil suction side for TL4 in Fig. 9). Later in the oscillation cycle, the flow re-attaches again and the shock wave moves downstream.

It is to be expected that a transitional situation between those alternative situations occurs. In the transitional situation the local power exchange around the shock position is close to zero. Oscillations could still be amplified, but they would obtain their energy from the flow mainly due to the dynamics of trailing-edge flow separation. In three cases, the shock wave may not contribute to the power exchange between fluid and structure. In the first, the shock wave moves in phase with the heave motion and thus out of phase with the heave velocity. In the second, the shock sticks on its steady state position, and in the third, a shock-free condition is reached. In any case, boundary-layer separation most likely is involved in order to provoke this shock-motion behavior at transonic speeds and/or in order to feed the energy into the observed oscillations. A further increase in Mach number should result in the above-described stabilizing effect of the shock-wave motion such that the flutter-speed index of the flutter boundary can increase with Mach number. Therefore, this transitional situation is expected to correspond to an inflection point in the flutter boundary. An example of an LCO in this transitional situation is the test case MP77 described by Schewe et al. (2003). MP77 is measured on the decreasing branch of the flutter boundary close to the transonic-dip minimum. Indeed, the shock wave nearly sticks on its position during the LCO, which is indicated to be related to slight flow separation (Schewe et al., 2003, p. 17).

Flow separation on supercritical airfoils, as here for the NLR 7301, is usually of type B according to the classification of Pearcy et al. (1968). Furthermore, it is very sensitive to the Reynolds number and to the boundary-layer transition location (Tijdeman, 1977). This fact, combined with the just described amplification mechanisms of the aeroelastic system close to the transonic-dip minimum, might help to understand the observation of Schewe et al. (2002, Fig. 3.2) that the transition location can affect the Mach number and the depth of the transonic-dip minimum significantly.

In conclusion, flow separation and its interaction with the shock wave most likely cause the increasing branch of the flutter boundary, such that a transonic-dip minimum occurs. Therefore, the transonic-dip minimum is observed to occur close to the lift-divergence Mach number (Schewe et al., 2003).

4.4. Impact on the numerical prediction of the transonic dip and LCOs

The present investigation confirms that the aeroelasticity close to the transonic dip is strongly determined by the transonic flowfield. In particular, the steady transonic flowfield on the airfoil with its supersonic regions, shock waves, and possible boundary-layer separation governs the unsteady airloads in case of airfoil oscillations and thus the observed aeroelastic behavior. In this manner the transonic flow has a strong nonlinear impact on the transonic aeroelasticity [cf. Tijdeman (1977), p. 19]. Nevertheless, the present data indicate that the linearization of the unsteady flow response on the airfoil oscillation is suitable for very small oscillations, e.g. $\hat{\alpha}$ in the order $\mathcal{O}(0.05^\circ)$. However, the observed LCOs demonstrate that the unsteady flow depends nonlinearly on the oscillation amplitudes, at least for higher oscillation amplitudes. Consequently, the unsteady transonic flow must be treated as nonlinear for high oscillation amplitudes although this nonlinearity is shown here to be weak. This means that the prediction of the flutter-stability boundary exhibiting a transonic dip requires accounting for the nonlinear steady transonic flowfield but might

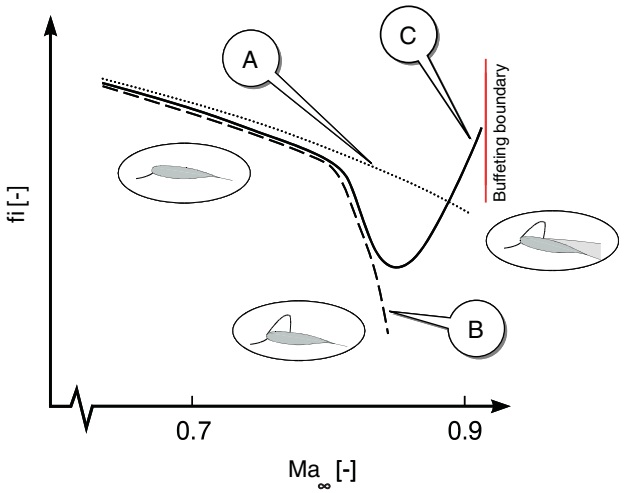

Fig. 13. A principle representation of a flutter boundary with a transonic dip which sketches the prediction capabilities of numerical methods.

use a linearized model for the unsteady airloads. However, the prediction of LCOs should, of course, not be possible using a conventional linearized model.

The impact of the above presented results on the expected prediction capabilities of numerical CAE methods to predict the aeroelastic behavior near the transonic dip is sketched in Fig. 13. In addition to linear or nonlinear methods, three basic types of methods are distinguished here.

A. Methods which in principle assume potential flow about infinitesimal thin lifting surfaces. Thus, these methods account for neither viscous effects nor the impact of the steady transonic flowfield with respect to thickness, camber or incidence of the wing. The most prominent example of such a method is the doublet-lattice method (DLM) (Albano and Rodden, 1969) which is designed for high subsonic but subcritical flow.
B. Methods based on the assumptions of the Euler- or potential-equations which themselves also neglect viscous effects. Nevertheless, these methods account for the impact of the steady transonic flowfield on the unsteady flow which is due to wing thickness, camber and/or incidence. Cost-efficient methods of this category are, e.g., the transonic equivalent strip (TES) method (Liu et al., 1988) or the transonic doublet-lattice method (TDLM) (Voß, 1985; Lu and Voß, 1993). High-fidelity methods of this type are Euler methods, e.g., used by Kholodar et al. (2003, 2004a, b). These methods are valid only for attached flow.
C. Methods that also take into account viscous/inviscid interaction. Potential- or Euler-equation based methods strongly coupled with a boundary-layer simulation[1] or Navier–Stokes-equation based methods are typical examples of this category. Such methods were used, e.g., by Weber et al. (2001), Castro et al. (2001), Tang et al. (2003), Thomas et al. (2003), Geissler (2003), Voß and Hippe (2006).

Methods of category A may lead to nonconservative results in the transonic region like sketched in Fig. 13 (cf. also flat-plate stability limit in Fig. 3). This is caused by the fact that the disturbance propagation in the mean transonic flowfield is strongly determined by the supersonic regions on the wing. The time lag of the unsteady flow response to the motion is often increased compared with the infinitesimal-thin-airfoil solution such that a shock wave exhibits a destabilizing effect. Therefore, methods of category B are able to capture the decreasing branch of the transonic dip at Mach numbers below that of the transonic-dip minimum [e.g. Euler-based results in Kholodar et al. (2004a) or TDLM-based results in Dietz et al. (2004b)]. However, even the use of a steady flow prediction including flow separation as base flow for a e.g. TDLM prediction will not enable one to predict the increasing branch of the transonic dip correctly (Dietz et al., 2004b). However, methods of category B which are not linearized, e.g. full Euler methods, should also be able to simulate LCOs near this branch in cases where only the shock-wave dynamics and not a viscous/inviscid

[1]Such simulations involving large trailing-edge separation often match fairly well experimental data, although the boundary-layer equations are restricted to flows with limited separation and weak wall-normal pressure gradients.

interaction cause the amplitude limitation (Bendiksen, 2004). Of course, methods of categories A or B will yield results also at high Mach numbers. Moreover, an increase of flutter-indices at higher Mach numbers might be observed, e.g. if a shock wave reaches the trailing edge of a wing. Nevertheless, from a technical point of view these predictions might be seen as artifacts in the sense that they may not represent the physics which occur with the real transport aircraft being operated at high but finite Reynolds numbers. Only the methods of category C are expected to predict the transonic-dip minimum and the increasing branch of the flutter boundary at higher Mach numbers as well as the buffeting boundary. These aeroelastic phenomena are determined by more or less strong viscous/inviscid interaction and separation which need to be modeled appropriately. Therefore, most of the LCO manifestations, as well, will demand a method of type C, which is not linearized, to be predicted satisfyingly.

The presented results regarding the aeroelastic self-excitation mechanisms in transonic flow, together with former observations (Dietz et al., 2004b), indicate the following: the disturbance propagation in the upstream direction above the airfoil suction side obviously strongly determines the time lag of the aerodynamic response to the wing motion. Therefore, the disturbance propagation above the shock wave needs to be simulated appropriately. Unfortunately, typical modern grid adaptation techniques might coarsen the grid in this region, since no strong gradients of the flow variables are generally present there. In our opinion, in addition to the shock wave and the boundary layer, this region needs to be spatially resolved such that the disturbance propagation is predicted with sufficient accuracy in order to capture the flutter boundary correctly.

The present investigation shows that the differences between the energy exchange while the amplitudes grow toward the LCO, or while the aeroelastic system falls back to the LCO, are small. Thus, if a CAE code is not able to model the energy exchange correctly with a sufficient accuracy, LCOs may not be detected or predicted with an unphysical amplitude. So, the present results confirm conclusion 2 of Bendiksen (2004).

Schuster et al. (2003) ask for a continuation of development of CAE methods on three levels of complexity. According to our knowledge, linear methods with the lowest complexity are actually only located in the categories A and B. Thus, they cannot predict the flutter or buffeting boundary at Mach numbers higher than that of the transonic-dip minimum. The discussion related to Fig. 11 might motivate a simple boundary-layer separation model which could be implemented in unsteady aerodynamic simulation methods like TDLM by Voß (1985); Lu and Voß (1993). In this way, a linearized cost-efficient method of category B might be extended to C such that it is able to predict the shape of the transonic dip.

5. Concluding remarks

Results from recent experiments on heave/pitch flutter of the supercritical airfoil NLR 7301 with tripped laminar-turbulent transition at transonic flow conditions have been reported. The tests were conducted in the Transonic Wind Tunnel Göttingen DNW-TWG using an adaptive-wall test section and a new flutter-test set-up. Flutter boundaries exhibiting a transonic dip have been measured for three angles of attack. Limit-cycle oscillations (LCOs) were identified close to the transonic dip. Two LCO cases were selected for further investigation. One LCO case was measured at a supercritical Mach number lower than that of the transonic dip, and another was obtained at a Mach number close to the buffeting boundary. Both cases are representative of the aeroelastic behavior on the increasing and decreasing branch of the transonic dip in the present tests. The local energy exchange between the fluid and the structure was examined from pressure distributions for those cases.

The most significant results of the present investigation can be summarized as follows.

(i) At supercritical Mach numbers below that of the transonic-dip minimum the presence of a shock-wave and its dynamics destabilizes the aeroelastic system such that the decreasing branch of the transonic dip develops.
(ii) At higher Mach numbers the shock-wave motion has a stabilizing effect such that the flutter boundary increases to higher flutter-speed indices with increasing Mach number. Self-excited oscillations near this branch of the flutter boundary obtain their energy from the fluid, mainly due to the dynamics of trailing-edge flow separation.
(iii) A slight nonlinear amplitude dependency of the shock-motion characteristics and possibly occurring boundary-layer separation cause the amplitude limitation of the observed LCOs.

The present results are obtained at mass ratios μ in the order of $\mathcal{O}(1000)$ which are high compared with real transport-aircraft configurations. Furthermore, the tests cover only a very limited range of structural-dynamic parameters. Therefore, it is not claimed that the results are generally transferable to a real transport aircraft. However, in our opinion the presented results are representative for the aeroelastic behavior close to the transonic dip according to our

experience (Schewe et al., 2002, 2003; Dietz et al., 2003, 2004a), since primarily the aerodynamics determines the aeroelastic behavior at these conditions. Please note that the aerodynamics are even more dominant compared with the structural dynamics for a real aircraft than in our experiments, since the ratio of aerodynamic work to total energy scales with $1/\mu$ [cf. Eq. (10) in Dietz et al. (2004a)]. However, the present results indicate the following consequences for the aeroelastic behavior of transport aircraft operated at high but finite Reynolds numbers.

(a) Methods like pure DLM would likely be unable to predict a transonic dip.
(b) Methods like TES, TDLM, pure potential- and Euler-equation based methods could predict the decreasing branch of the transonic dip.
(c) Only methods which account for viscous/inviscid interaction including flow separation are expected to predict the increasing branch of the transonic dip and thus the transonic-dip minimum correctly.
(d) The results indicate that the "stability" of stable LCOs is rather weak: there are only small differences between the energy exchange while the amplitudes grow toward an LCO or while the aeroelastic system falls back to an LCO. This confirms the authors' opinion (Dietz et al., 2004a) that LCOs are only marginally usable as a fall-back position while using an active damping system in order to extend the operational flight regime of an aircraft.
(e) Subcritical bifurcations as described by Dowell et al. (2003, Scenario 1) were again identified in the present investigation. This nonlinear aeroelastic behavior is technically important since traditional flutter-stability analysis only investigates the response of the aeroelastic system to infinitesimal small disturbances. However, gusts or strong control commands may push the aeroelastic system from one state without oscillations to another safety-critical state with strong oscillations, which could not be detected by the traditional aeroelastic analysis. Therefore, a strategy for a safe but time-efficient aeroelastic analysis is needed that includes looking for subcritical bifurcations. However, an appropriate aeroelastic modeling of this phenomenon requires accounting for the impact of the steady, relatively strong, nonlinear transonic flowfield on the unsteady, relatively weak, nonlinearairloads.

The present results relate the local aerodynamics to the observed amplification and amplitude limitation of aeroelastic oscillations close to the transonic dip. Based on this physical understanding, we intend to improve the numerical prediction capabilities of the observed phenomena, in particular regarding the transonic dip and subcritical bifurcations. Furthermore, we intend to derive measures aiming to reduce the collapse of the flutter boundary at the transonic dip. These measures could be useful to improve the performance and to ensure the safe operation of future transport aircraft.

Acknowledgments

We are grateful to Professor Dr V. Carstens for providing the code to solve the Possio integral equation and wish to thank Dr W. Geissler, Dr F. Kießling, Dr R. Voß, and J. Agte for fruitful discussions and suggestions. Thanks to R. Bakker for preparing the energy-balance evaluation. Thanks also to J. Nuhn for thoroughly acquiring the data as well as to J. Berold and D. Möhle being responsible for the models and the test set-ups. Finally, we would like to thank the staff of the DNW-TWG for their cooperation. This work was supported by the basic founding of the German Aerospace Center DLR.

References

Akima, H., 1970. A new method of interpolation and smooth curve fitting based on local procedures. Journal of the ACM 17, 589–602.
Albano, E., Rodden, W.P., 1969. A doublet-lattice method for calculating lift distributions on oscillating surfaces in subsonic flow. AIAA Journal 7, 279–285.
Bendiksen, O.O., 1992. Role of shock dynamics in transonic flutter. AIAA Paper 92-2121.
Bendiksen, O.O., 1999. Improved similarity rules for transonic flutter. AIAA Paper 99-1350.
Bendiksen, O.O., 2001. Transonic flutter and the nature of the transonic dip. In: Proceedings of International Forum on Aeroelasticity and Structural Dynamics, vol. 2, Madrid, Spain, pp. 273–286.
Bendiksen, O.O., 2004. Transonic limit cycle flutter/lco. AIAA Paper 2004-1694.
Birnbaum, W., 1924. Der Schlagflügelpropellor und die kleinen Schwingungen elastistisch befestigter Tragflügel. ZFM 15, 128–134.
Carstens, V., 1973. Berechnung der instationären Druckverteilung an harmonisch schwingenden Gittern in ebener Unterschallströmung. IB 253-73 J06, DLR.

Castro, B.M., Ekaterinaris, J.A., Platzer, M.F., 2001. Analysis of the effect of porous wall interference on transonic airfoil flutter. AIAA Paper 2001-2725.

Cebeci, T., Bradshaw, P., 1979. Momentum Transfer in Boundary Layers. McGraw-Hill, New York.

Chen, P.C., Sarhaddi, D., Liu, D.D., 1998. Limit cycle oscillation studies of a fighter with external stores. AIAA Paper 98-1727.

Dietz, G., Schewe, G., Kießling, F., Sinapius, M., 2003. Limit-cycle-oscillation experiments at a transport aircraft wing model. In: Proceedings of International Forum on Aeroelasticity and Structural Dynamics, Amsterdam, The Netherlands.

Dietz, G., Schewe, G., Mai, H., 2004a. Experiments on heave/pitch limit-cycle oscillations of a supercritical airfoil close to the transonic dip. Journal of Fluids and Structures 19, 1–16.

Dietz, G., Voß, R., DeBreuker, R., 2004b. Airfoil optimization based on an evolution strategy with respect to aeroelasticity. In: Proceedings European Congress on Computational Methods in Applied Sciences and Engineering ECCOMAS, vol. II, University of Jyväskylä, Jyväskylä, Finland.

Dowell, E.H., Edwards, J., Strganac, T., 2003. Nonlinear aeroelasticity. Journal of Aircraft 40, 857–874.

Drela, M., 1990. Newton solution of coupled viscous/inviscid multielement airfoil flows. AIAA Paper 90-1470.

Drela, M., Giles, M.B., 1987. Viscous-inviscid analysis of transonic and low Reynolds number airfoils. AIAA Journal 25, 1347–1355.

Geissler, W., 2003. Numerical study of buffet and transonic flutter on the NLR 7301 airfoil. Aerospace Science and Technology 7, 540–550.

Grüber, B., Carstens, V., 2001. The impact of viscous effects on the aerodynamic damping of vibrating transonic compressor blades—a numerical study. ASME Journal of Turbomachinery 123, 409–417.

Jacobs, M., 2002. Treatment of the wall boundary layer in the wall adaptation procedure and steady wall adaptation for dynamic tests, private communication, DNW BU GuK, Göttingen.

Kholodar, D.B., Thomas, J.P., Dowell, E.H., Hall, K.C., 2003. Parametric study of flutter for an airfoil in inviscid transonic flow. Journal of Aircraft 40, 303–313.

Kholodar, D.B., Dowell, E.H., Thomas, J.P., Hall, K.C., 2004a. Improved understanding of transonic flutter: a three-parameter flutter surface. Journal of Aircraft 41, 911–917.

Kholodar, D.B., Dowell, E.H., Thomas, J.P., Hall, K.C., 2004b. Limit-cycle oscillations of a typical airfoil in transonic flow. Journal of Aircraft 41, 1067–1072.

Knipfer, A., Schewe, G., 1999. Investigation of an oscillating supercritical 2D wing section in transonic flow. AIAA Paper 99-0653.

Liu, D.D., Kao, Y.F., Fung, K.Y., 1988. An efficient method for computing unsteady transonic aerodynamics of swept wings with control surfaces. Journal of Aircraft 25, 25–31.

Lu, S., Voß, R., 1993. TDLM—a transonic doublet lattice method for 3-D potential unsteady transonic flow calculation and its application to transonic flutter prediction. In: Proceedings of International Forum on Aeroelasticity and Structural Dynamics, vol. 1, Strasbourg, France, pp. 77–95.

Mignolet, M.P., Liu, D.D., Chen, P.C., 1999. On the nonlinear structural damping mechanism of the wing/store limit cycle oscillation. In: Proceedings 40th Structures, Structural Dynamics, and Materials Conference, vol. 3, St Louis, Missouri, USA, pp. 2148–2161.

Patil, M.J., 2002. Limit cycle oscillations of aircraft due to flutter-induced drag. AIAA Paper 2002-1409.

Patil, M.J., 2003. From fluttering wings to flapping flight: the energy connection. Journal of Aircraft 40, 270–276.

Pearcy, H.H., Haines, A.B., Osborne, J., 1968. The interaction between local effects at the shock and rear separation. AIAA Paper CP 35, AGARD.

Rivera, J.A., Dansberry, B.E., Bennett, R.M., 1992. NACA 0012 benchmark model experimental flutter results with unsteady pressure distributions. AIAA Paper CP 92-2396.

Schewe, G., 1991. Force measurements in aeroelasticity using piezoelectric multicomponent transducers. In: Proceedings of International Forum on Aeroelasticity and Structural Dynamics, DGLR 91-06, Aachen, Germany.

Schewe, G., Deyhle, H., 1996. Experiments on transonic flutter of a two-dimensional supercritical wing with emphasis on non-linear effects. In: Proceedings RAeS Conference on "Unsteady Aerodynamics", London, UK.

Schewe, G., Knipfer, A., Mai, H., Dietz, G., 2002. Experimental and numerical investigation of nonlinear effects in transonic flutter. IB 232-2002, DLR.

Schewe, G., Mai, H., Dietz, G., 2003. Nonlinear effects in transonic flutter with emphasis on manifestations of limit cycle oscillations. Journal of Fluids and Structures 18, 3–22.

Schuster, D.M., Liu, D.D., Huttsell, L.J., 2003. Computational aeroelasticity: success, progress, challenge. Journal of Aircraft 40, 843–856.

Stanewsky, E., 1990. Experimental investigation of buffet onset and penetration on a supercritical airfoil at transonic speeds. CP 483, AGARD.

Tang, L., Bartels, R.E., Chen, P.C., Liu, D.D., 2003. Numerical investigation of transonic limit cycle oscillations of a two-dimensional supercritical wing. Journal of Fluids and Structures 17, 29–41.

Thomas, J.P., Dowell, E.H., Hall, K.C., 2003. Modeling limit cycle oscillations for an NLR 7301 airfoil aeroelastic configuration including correlation with experiment. AIAA Paper 2003-1429.

Thomas, J.P., Dowell, E.H., Hall, K.C., 2004. Modeling viscous transonic limit-cycle oscillation behaviour using a harmonic balance approach. Journal of Aircraft 41, 1266–1274.

Tichy, L., Henke, H., 1993. Unsteady transonic pressures on a NACA 0012 airfoil and their effect on flutter stability. In: Proceedings of International Forum on Aeroelasticity and Structural Dynamics. Strasbourg, France.

Tijdeman, H., 1977. Investigations of the transonic flow around oscillating airfoils. Diss., Technische Hogeschool Delft, The Netherlands, also NLR TR 77090.

Tijdeman, H., Seebass, R., 1980. Transonic flow past oscillating airfoils. Annual Review of Fluid Mechanics 12, 181–222.

Voß, R., 1985. Calculation of 3-D unsteady transonic potential flows by a field panel method. In: Proceedings of International Forum on Aeroelasticity and Structural Dynamics, DGLR Bericht 85-02, pp. 33–46.

Voß, R., 1998. Wall correction methods for dynamic tests. AG 336, AGARD.

Voß, R., Hippe, C., 2006. Computation of the flutter boundary of the NLR 7301 airfoil in the transonic range. In: Notes on Numerical Fluid Mechanics and Multidisciplinary Design, vol 92, Springer, Berlin.

Weber, S., Jones, K.D., Ekaterinaris, J.A., Platzer, M.F., 2001. Transonic flutter computations for the NLR 7301 supercritical airfoil. Aerospace Science and Technology 5, 293–304.

Wedemeyer, E., Taylor, N.J., Holst, H., 1998. Adaptive wall techniques. AG 336, AGARD.

Zwaan, R.J., 1979. Summary of data required for the AGARD SMP activity "Standard Aeroelastic Configurations"—two-dimensional configurations. MP 79015 U, NLR.